This is a preprint, the final version is subject to change, of the American Mineralogist (MSA)
Cite as Authors (Year) Title. American Mineralogist, in press.
DOI: https://doi.org/10.2138/am-2018-6508

Revision 1

Is fibrous ferrierite a potential health hazard?

Characterization and comparison with fibrous erionite

ALESSANDRO F. GUALTIERI[1*], NICOLA BURSI GANDOLFI[1], ELIO PASSAGLIA[1], SIMONE POLLASTRI[2], MICHELE MATTIOLI[3], MATTEO GIORDANI[3], MARIA FRANCESCA OTTAVIANI[3], MICHELA CANGIOTTI[3], ANDREA BLOISE[4], DONATELLA BARCA[4], RUGGERO VIGLIATURO[5], ALBERTO VIANI[6], LUCA PASQUALI[7] AND MAGDALENA LASSINANTTI GUALTIERI[7]

[1]Dipartimento di Scienze Chimiche e Geologiche, Università degli studi di Modena e Reggio Emilia, I-41125, Modena, Italy

[2]Elettra-Sincrotrone Trieste, I-34149, Basovizza Trieste, Italy

[3]Dipartimento di Scienze Pure e Applicate, Università di Urbino *Carlo Bo*, I-61029 Urbino (PU) Italy

[4]Dipartimento di Biologia, Ecologia e Scienze della Terra, Università della Calabria, I-87036 Arcavacata di Rende (CS), Italy

[5]Laboratory for Material Chemistry, National Institute of Chemistry, S-1000 Ljubljana, Slovenia and Department of Earth and Environmental Science, University of Pennsylvania, 240 S. 33rd Street, Hayden Hall, Philadelphia, PA 19104-6316, U.S.A

[6]Institute of Theoretical and Applied Mechanics of the Czech Academy of Sciences, Centre of Excellence Telč, CZ-58856 Telč, Czech Republic

[7]Dipartimento di Ingegneria "Enzo Ferrari", Università degli studi di Modena e Reggio Emilia, I-41125, Modena, Italy

ABSTRACT

Fibrous erionite is classified by the IARC (International Agency for Research on Cancer) as carcinogenic substance to humans (Group 1). In the areas where it is present in the bedrock, it may cause environmental exposure, and both professional and environmental exposures is possible when the

bedrock is used for industrial applications (e.g. building materials). For the health and environment protection, prevention is a priority action. In this frame, the recent guidelines of the Consensus Report of the Weinman International Conference on Mesothelioma suggest to identify locations where potentially hazardous mineral fibers (like erionite) are found in the environment, to prevent environmental exposure. The present study will show that one such potentially hazardous mineral fiber might be fibrous ferrierite. Here, the mineralogical, chemical-physical properties and surface activity of a hydrothermal fibrous ferrierite from Monte Lake British Columbia (Canada) and a diagenetic fibrous ferrierite from Lovelock Nevada (USA) were investigated using a combination of 'state of the art' experimental methods including optical microscopy, electron microscopy and microprobe analysis, laser ablation inductively coupled plasma mass spectrometry for the trace elements, vibrational spectroscopy, electron paramagnetic resonance, and synchrotron powder diffraction. The chemical-physical properties of these fibrous ferrierites (morphometric parameters, specific surface area, chemical composition with special attention to metals, mainly iron) prompting adverse effects *in vivo* were compared to those of the positive carcinogenic standard fibrous erionite-Na from Jersey Nevada (USA). The results of our study have demonstrated that, although there are differences in the crystal chemistry and genetic environment, ferrierite samples exhibit outstanding similarities with fibrous erionite samples: both fibrous erionite and fibrous ferrierite may occur in large amounts as microcrystalline fibrous-asbestiform phases in diagenetic rocks with fibers of breathable sizes. For both zeolites, iron is not structural but is associated with impurities lying at the surface of the fibers. Moreover, data useful to understand the surface activity of these fibrous ferrierites were collected. As far as hydrothermal sample is concerned, the EPR data indicate the presence of hydrophilic (SiO-, AlO-, SiOH) and hydrophobic (Si-O-Si) interacting surface groups able to bind the charged CAT1 probes at close sites and attract the probes in the water pools formed into the fiber aggregates. A high percentage of CAT1 probes weakly interacting with the surface due to competition with metal ions was observed

for surface of the diagenetic sample. CAT8 probes were less adsorbed by its surface if compared to the diagenetic sample but the more charged surface provided a stronger binding strength for the diagenetic sample compared to the hydrothermal one. In summary, the results of this study indicate that fibrous ferrierite may represent a potential health hazard and, applying the precautionary principle, it should undergo a procedure of toxicity testing.

Keywords: Zeolite, ferrierite, erionite, mineral fiber, health hazard.

INTRODUCTION

The mineral ferrierite was found for the first time by W.F. Ferrier in altered basalts of early Miocene age from the north shore of Kamloops Lake, British Columbia, Canada and was studied by Graham (1918) who named the mineral. Ferrierite, with chemical formula $(Mg_{0.5},Na,K)_6[Al_6Si_{30}O_{72}]\cdot 20H_2O$ (Passaglia and Sheppard 2001), belongs to the mordenite group of zeolites (Gottardi and Galli 1985) and displays a framework type **FER** with a 2-dimensional channel system and 5-1 secondary building units assembling 5-, 6-, 8-, 10-membered rings (Baerlocher et al. 2007). The mineral is one of the most siliceous naturally occurring zeolites. Several zeolites with the **FER** type framework have also been synthesized (Fjellvåg et al. 1989) and successfully used as versatile catalysts both in hydrocarbon processing and in the petrochemical industry (Pickering et al. 1989).

The crystal structure of natural Mg-dominant ferrierite was determined from single crystal X-ray data by Vaughan (1966) and Kerr (1966) and confirmed later by Gramlich-Meier et al. (1984) and Alberti and Sabelli (1987) in space group *Immm* or *Pmmm*. A monoclinic $P2_1/n$ variant of Na-dominant ferrierite is also known (Gramlich-Meier et al. 1985). The unit cell parameters are a=18.90-19.45 Å, b=14.12-14.28 Å and c=7.48-7.54 Å (Passaglia and Sheppard 2001). Vaughan (1966) found a slight enrichment of Al in the tetrahedra of the 6-membered rings between the hexagonal sheets parallel to the

(100). The Mg atoms are coordinated to six water molecules whereas the Na cations are found in the main channel parallel to the **c** axis and surrounded by the 10-membered rings.

Ferrierite has mainly been found in voids of volcanic rocks (hydrothermal origin) coexisting with other zeolites (e.g., heulandite, dachiardite, mordenite, analcime, chabazite, harmotome), carbonates, barite, apatite, pyrite, cinnabar, and chalcedony (Passaglia and Sheppard 2001). Ferrierite has also been found in tuffaceous sediments (diagenetic origin) coexisting with mordenite, clinoptilolite, feldspars and quartz. An example of a major occurrence of ferrierite as a diagenetic product of volcanic (Tertiary rhyolitic pyroclastic) rocks is at the deposit of Lovelock, Nevada USA (Rice et al. 1992) where its content is >50 wt% (zeolite-rich rock) and hence high enough for mineral exploitation. This mode of occurrence stimulated studies in agricultural and industrial applications (see for example Townsend and Loizidou 1984). In both hydrothermal and diagenetic occurrences, ferrierite may exhibit different crystal habits (lath-like/lamellar, prismatic, needle-like, acicular, fibrous, and asbestiform: see for example Rice et al. 1992). A large amount of microscopic ferrierite crystals with fibrous-asbestiform habit is observed in diagenetic rocks that can eventually be mined and used for industrial applications. This may raise some concerns due to the close resemblance with fibrous erionite which is known to induce malignant mesothelioma (MM). As a matter of fact, diagenetic erionite crystallizes as needle-like fibers with widths from nanometric to micrometric. Larger bundles of these crystals are also common. Disturbance of the friable host rocks can generate airborne fibers with physical dimensions similar to asbestos fibers (Harper et al. 2017) and like asbestos, such fibers may represent a severe environmental and health hazard. A paradigmatic example of this kind is represented by the "Cappadocia case": the residents of the Turkish villages of Karain, Sarihidir and Tuzkoy, where the fibrous erionite-containing rock was used as building stone in home construction, have a remarkably high risk for developing MM (Carbone et al. 2011). The concern with the carcinogenic potential of erionite has sparked an interest within areas of the US where fibrous erionite is found in regional

bedrock or sediments (Saini-Eidukat and Triplett 2014). These areas include formations scattered across western North Dakota, South Dakota, and Montana (Goodman and Pierson 2010). There is a concern with exposure and transmission of airborne dust and particulate, possibly containing erionite fibers, from gravel pits, roads, parking lots, playgrounds, feed lots, building and construction, mining operations, oil extraction, and farming/ranching operations (Carbone et al. 2011).

Prompted by the recent guidelines of the Consensus Report of the Weinman International Conference on Mesothelioma (Carbone et al. 2016) that suggest to identify locations where potentially hazardous mineral fibers are found in the environment, here we have investigated the mineralogy, the chemical-physical properties and the surface activity of fibrous ferrierite from Monte Lake British Columbia (Canada) of hydrothermal origin and fibrous ferrierite from Lovelock Nevada (USA) of diagenetic origin.

The characteristics of these fibrous zeolites were compared to those of diagenetic fibrous erionite-Na from Jersey Nevada (USA), considered a positive carcinogen. The comparison of the chemical-physical properties prompting adverse effects *in vivo* with those of the known carcinogen fibrous erionite is pivotal to assess if fibrous ferrierite may also represent a potential health hazard.

EXPERIMENTAL

The fibrous ferrierite selected for the study is from Monte Lake, southeastern Kamloops District, British Columbia (Canada). This mineral occurs in the voids of basalt flows belonging to the middle Tertiary Kamloops Group (Jones 1959). The ferrierite crystals are found in vesicles and calcite-filled nodules in a fine-grained, greenish-black basalt composed of microphenocrystals of labradorite and augite set in an opaque glass matrix. The basalt is situated in a large road cut east of Monte Lake and along railway cuts one-mile south of the lake (Wise and Tschernich 1976). The ferrierite occurs as colorless to salmon-colored thin blades, needles, fibrous aggregates of various size. Ferrierite fibers

were manually separated from the matrix under a stereoscopic optical microscope. Different samples were used depending on the experimental method applied: fibers inside the bulk matrix (e.g., for micro-Raman analysis); a representative selection of ferrierite fibers (e.g., for EMPA); bulk powder sample ground into an agate mortar (e.g., for X-ray diffraction experiments). The code assigned to this sample is BC.

The diagenetic fibrous ferrierite sample is from Lovelock (Nevada). The Lovelock deposit occurs in a group of sedimentary and volcanic rocks (rhyolitic pyroclastites) of Tertiary age (Miocene or Pliocene) in a small valley within the Trinity Range (T. 28 N., R. 30 E.) in Pershing County, northwest Nevada (Rice et al. 1992). Ferrierite is accompanied by mordenite, clinoptilolite and other minerals like orthoclase and cristobalite. Ferrierite has formed with smectite through hydration reactions of the rhyolitic pyroclastites from high activities of silica and magnesia required simultaneously for the large-scale crystallization of ferrierite in these diagenetically altered rocks. Post-depositional addition of Mg coincided with ferrierite and smectite formation (Rice et al. 1992). The content of the zeolite phases is > 50 w% and hence the pyroclastic rock can be classified as the zeolite-rich raw material of mining and commercial interest (Gualtieri et al. 1999). Unfortunately, it was not possible to manually separate single fibers under a microscope as was done for the BC sample. The crystals were too small in this case. Hence, analyses were performed either on fibers inside the bulk matrix or on the bulk powder sample ground into an agate mortar. The code assigned to this sample is LN.

The BC and LN raw samples were observed by stereomicroscopy of low resolution as well as by PLOM. The latter provides a non-destructive way to verify the crystal habit of a mineral with relatively high spatial resolution. The investigation was performed in transmitted light with an Olympus BH-2 microscope.

SEM analyses were performed using a FEI Nova NanoSEM 450 FEG-SEM equipped with a X-EDS Bruker QUANTAX-200 system, with 15kV accelerating voltage and 3.5μA beam current. BC and LN

samples were mounted on a Al stub and gold coated (10 nm of thickness). Both back-scattered (BSE) and secondary electron (SE) images were recorded.

TEM/STEM investigations were conducted using a JEOL-ARM 200 F with a CFEG (Cold Field-Emission Gun) operating at 80 kV and equipped with a probe spherical aberration corrector (Cs), allowing atom-resolved imaging in STEM high angle annular dark field (HAADF) mode. The microscope was equipped with an Energy-Dispersive X-ray Spectroscopy(EDS) system (Centurio 100 mm^2, JEOL) and a Quantum GIF (Gatan, USA) for Electron Energy-Loss Spectroscopy, with Dual EELS capability. A Cryo-transfer holder, operating at ≈-178 °C was used to avoid heating, beam damages and stabilize the specimen under the electron beam. The use of Dual EELS allows to remove the energy shift (using the low-loss spectra as control) avoiding the need of subsequently measure the low-loss and high-loss spectra, and was used to determine the iron oxidation state down to the atomic scale using three different methods (applied on the core-loss region), namely: direct comparison with standards reference spectra, modified integral Fe L_{23} white-line intensity ratio (Tan et al. 2012) and ΔE method (Rojac et al. 2017). The spectra were collected using an aperture of 5 mm and a dispersion of 0.25 eV/ch. The low-loss spectra were registered over a time of 0.005 s and the core-loss spectra over a time of 20 s.

EMPA for quantitative determination of the chemical composition were performed using a JEOL 8200 Super Probe instrument with W hairpin type filament and minimum accelerating voltage of 30 kV. Analyses were performed on accurately selected fibers (using a stereomicroscope, see above) so that estimates should be highly reliable. The final chemical composition is the mean value of 10 spot analyses carried out on various fibers. The calculation of the crystal-chemical formula was normalized on the basis of 72 O.

For the determination of structural water, a thermo-gravimetric (TG) measurement was performed on the BC sample using a simultaneous differential thermal analysis (SDTA) SEIKO SSC/5200 SII.

Data were collected in the air with a flow rate of 2 μL/min, in the range 25-1150 °C, and a heating rate of 10 °C/min.

LA-ICP-MS was used to measure minor and trace elements with spot resolutions of about 40–50 μm on sections with a thickness of about 1mm of samples embedded on epoxy resin constituted by aggregates of selected fibers in the case of the BC sample and fibers inside the bulk matrix in the case of the LN sample. Using this technique, micrometric compositional variations can be studied. Analyses were carried out using an Elan DRCe instrument (Perkin Elmer/SCIEX) connected to a New Wave UP213 solid- state Nd-YAG laser probe (213 nm). Data collection was possible by using the common experimental procedure used in the Mass Spectroscopy Laboratory (e.g., Barca and Trua 2012). In detail, samples were ablated by a laser beam in a cell, under a moderate flow of pure helium. Behind the cell, the ablated material was flushed in a continuous flow of a helium and argon mixture to the ICP system, where it was atomized and ionized for quantification in the mass spectrometer. The initial alignment of the instrument was performed through nebulization of the solution whereas a second optimization step was obtained using "NIST612-50 mg g 1 glass" reference material. In this work, ablation was performed with spots of 40 μm, with a constant laser repetition rate of 10 Hz and a flow of 20 J/cm^2. In particular, for all analyses, a transient signal of intensity vs. time was obtained for each element using a 60 s background level (acquisition of gas blanks) followed by 40 s of ablation and then 60 s of post-ablation at background levels. Data were processed by the Glitter program. In this study, seven spot analyses were performed on each sample. The data collection strategy included the "USGS BCR 2G glass" reference material as an unknown sample. Element concentrations obtained for the analyses executed on control standards were compared with reference values from the literature. The accuracy (i.e., the relative difference from reference values) was generally better than 12% and most elements plotted in the range 8%. Internal standardization to correct instrumental instability and drift was achieved with CaO concentrations from microprobe analyses.

XRPD patterns of both BC and LN samples used for the qualitative phase analysis were collected at the MCX beamline at ELETTRA (Trieste, Italy) using a Debye-Scherrer geometry and a wavelength of 1.0324 Å. The sample powders were inserted in a borosilicate 0.3 mm diameter capillary that was spun during data collection. The structure refinements of the two samples are out of the aims of this paper but will be the subject of an exclusive work also including the analysis of the stacking fault defectivity.

FTIR analyses were performed on sample powders in the spectral range 500–4000 cm^{-1} using a Bruker Vertex 70 spectrometer equipped with a Specac Golden Gate sample holder, operating in reflection geometry. Micro-Raman spectra in the range 1800–50 cm^{-1} were collected on single BC and LN fibers embedded in the sample matrix using a DXR Raman spectrometer (Thermo Scientific) equipped with a 1024×256 CCD detector, at laser wavelength 532 nm, high-resolution grating (1800 lines mm^{-1}) with nominal resolution (FWHM) of 2 mm^{-1} and 50 cm^{-1} Rayleigh Rejection Filter (Stokes shift). The laser beam (diameter about 0.6 μm) was focused with a 100× objective (Numerical Aperture = 0.90). The power applied on the sample was 10 mW.

XPS measurements were conducted using a CMA Perkin Elmer, 15-255-G with a XR3 double anode MgKα and AlKα sources, energy = 15kV, current = 18 mA. The spectra were collected using a double step cylindrical analyzer, with a step energy of 50 eV for high resolution spectra and a step energy of 100 eV for extended spectra.

To analyze the interacting ability of the zeolite surfaces, computer aided analyses of the electron paramagnetic resonance (EPR) spectra using selected spin probes were performed. This technique was already demonstrated to be a very useful tool, providing unique information about surface and interfacial properties (Mattioli et al. 2016). In the present case, this information is also precious because it may be related to the eventual carcinogenicity of the fibrous zeolites. The spin probes 4-trimethylammonium, 2,2,6,6 tetramethyl-piperidine-1oxyl Bromide (termed CAT1) and 4-octyl dimethylammonium, 2,2,6,6 tetramethyl-piperidine-1oxyl Bromide (termed CAT8) were selected since

they have been successfully employed in previous investigations of similar systems. Here, the main goal is to compare the results from the ferrierite samples with those previously obtained using the same spin probes to analyze the interacting ability of erionite, offretite and scolecite zeolite fibers (Mattioli et al. 2016). The samples for the EPR analyses were prepared by equilibrating overnight 200 mg of each zeolite with 0.5 ml of 1 mM aqueous (Millipore) solutions of CAT1 (Sigma-Aldrich) and CAT8 (donated by Dr. Xuegong Lei, Columbia University, NY, USA). In the next step, the suspensions were filtered and the filtrates were loaded in 2 mm tubes and analyzed by EPR under controlled and reproducible conditions to allow reliable evaluations of the spectral intensities. The stock solutions of CAT1 and CAT8 were also analyzed under the same experimental conditions as the filtrates to evaluate the intensity differences in the EPR spectra. The solid samples, separated from the probe solutions and directly dried on the filter paper, were analyzed as well. The spectra were acquired using an EMX-Bruker spectrometer operating at X band (9.5 GHz). The temperature was set to 298 K and controlled with a Bruker ST3000 variable-temperature assembly cooled with liquid nitrogen. Temperature scans were also performed to verify the adsorption conditions. In all cases, the reproducibility of the results was checked by repeating the EPR analysis at least three times in the same experimental conditions for each sample. Simulation of the EPR line shape was performed by using the program of Budil et al. (1996). The main parameters extracted from computation were: (a) the A_{zz} component (accuracy ± 0.05 G) of the hyperfine coupling tensor A for the coupling between the electron spin (S=1/2) and the nitrogen nuclear spin (I=1; n. of lines= 2I+1=3). For simplicity, we kept the A_{xx} and A_{yy} values constant (= 6 G). A_{zz} increases with increasing environmental polarity of the spin probe; (b) the correlation time for the rotational diffusion mobility of the spin probe (τ, accuracy ± 0.01 ns). τ increases with the increase of the local microviscosity, corresponding to an increase of probe-surface strength of interaction; (c) the line width (LW) (accuracy ± 0.01 G) increases with increasing spin-spin interactions and with increasing number of probes close to each other that interact with surface sites. In

several cases, the spectra are constituted by different components superimposing each other, due to probes distributed in different environments. The components were extracted by subtracting experimental and/or computed spectra from each other. Then, each component was computed to obtain the above-listed parameters. The subtraction procedure allowed us to quantify (in relative percentages, accuracy ± 1 %) the fractions of probes distributed in the different environments.

SSA of the BC and LN samples was determined from gas adsorption data recorded by a Gemini-V instrument and with N_2 as probe gas. Analyses were performed on samples conditioned at 105 °C as well as on samples conditioned at 350 °C. The SSA of the natural sample (conditioned at 105 °C) was determined with the BET model whereas the external surface area of the dehydrated sample (conditioned at 350 °C) was determined with the t-plot method.

The ξ potential was determined both in distilled water and in organic Gamble's modified solution (Guldberg et al. 1998), the latter reproducing the extracellular and intracellular macrophage phago-lysosome environment. The measurements were conducted in the pH range 3–10 at 37 °C (body T), using a ZetasizerNano Series instrument (Malvern). The pH of the suspensions was monitored using a Criston Series 2000 instrument.

RESULTS AND DISCUSSION

Characterization of fibrous ferrierites

Microscopic characterization

A stereomicroscopic study of the two fibrous ferrierite samples selected for the study was preliminarily performed. The hydrothermal sample BC displays visible aggregates of acicular/fibrous crystals with a light orange color (Fig. 1) whereas no crystals of the diagenetic sample LN can be observed.

Fig. 2 reports a selection of SEM pictures and relative EDS spot analyses of both BC and LN samples. The BC sample contains ferrierite crystals with both prismatic (Fig. 2a) and fibrous asbestiform shape (Fig. 2b, see the dashed line indicating flexible asbestiform fibers). BC ferrierite contains breathable (regulated) fibers according to the WHO (1997) counting criteria (particles with length ≥ 5 μm, width ≤ 3 μm, length/width ratio $\geq 3:1$). Fig. 2c shows that microparticles enriched in iron (see the EDS spectrum in Fig. 2e compared to that collected for the bulk in Fig. 2f) are present on the surface of the fibers. Such particles are likely iron-oxides/hydroxides. The LN sample also contains ferrierite crystals with fibrous asbestiform shape (Fig. 2d with the dashed line indicating flexible asbestiform fibers) and breathable fibers (WHO 1997).

The presence of iron-rich (presumably iron-oxides/hydroxides) nanophasic clusters or single nanophasic particles at the surface of the BC ferrierite fibers was revealed by high-resolution TEM investigations (Fig. 3a,b with the relative EDS spectra in Fig. 3c,d. Note that the spectra relative to the iron-rich particles are identical). STEM-HAADF (high angle annular dark field) technique combined with Dual-EELS was also applied to the BC sample. Fig. 3e represents a HAADF picture of a ferrierite fiber with a lighter region and spread clusters, witnessing the presence of iron-rich nanoparticles. The EELS low-loss spectra analysis (Malis et al. 1988) performed in this region showed that the right side of the fiber is slightly thicker (≈26 nm) if compared to the left part (≈20 nm). Fig. 3f represents the same area with a higher magnification, showing two brighter spots in the top right of the field with a radius comparable to that of a single atom (≈123 pm). To identify the nature of these clusters, STEM_HAADF combined with Dual-EELS was performed to collect low-loss and core-loss region spectra simultaneously, thus allowing to determine the iron oxidation state at this scale (Fig. 3g). The iron valence state was determined by comparison with standards ($FeTiO_3$ for Fe^{2+}; $Co_{0.6}Fe_{2.4}O_4$ for $Fe^{2.7+}$ and Fe_2O_3 for Fe^{3+}), using three different approaches, applied on the mean of 5 analysis points:

(a) comparison of the $Fe2p_{1/2}$ satellites and $Fep_{3/2}$ peak positions with an iron-rich reference; the values for the $Fe2p_{1/2}$ satellite and the $Fep_{3/2}$ peak are similar to the standard spectrum collected (on the same instrument) for $Co_{0.6}Fe_{2.4}O_4$ corresponding to a mean oxidation number of 2.7+. Notwithstanding, our specimen shows a slightly more pronounced satellite peak at 715.57eV in respect to the spectrum of reference.

(b) comparison of the modified integral Fe L_{23} white-line intensity ratio (double arc tangents method) with reference standard values; applying the second approach, a Fe-L_3/L_2 intensity ratio of 4.45 (σ=0.41) which correspond to a mean iron oxidation state of 2.7+ was found (The standard reference value for the same oxidation number is: 4.10 σ=0.30).

(c) comparison of the energy onset difference (ΔE) between the O-K and Fe-L_3 edges; the mean Fe-L_3 O-K onset difference for our specimen corresponds to 177.68 (σ=0.45) eV compatible with the energy onset difference of the standard $Co_{0.6}Fe_{2.4}O_4$ (ΔE=177.50 σ=0.45; Fe valence state of 2.7+).

All the three applied methods yield to a resulting mean oxidation state of the iron clusters at the surface of ferrierite fibers correspondent to $Fe^{2.7+}$.

These methods give the same result and are in accordance with the XPS outputs (which on the other hand provides a better statistics), but the higher spatial resolution of Dual-EELS allowed us to localize precisely the clusters on the fiber surfaces and their morphology, which made this technique an important contribution in the detailed description of potentially toxic mechanisms. The direct comparison of spectra, due to the possible presence of background disruptions, could lead to misinterpretation of satellite peak presence and height. In our case, the presence of the satellite peak let us suspect a possible deviation of the oxidation state from the discrete value of 2.7+ given by the direct comparison with the standard. Evaluating this aspect and the fact that the ΔE method is particularly suitable for the determination of iron oxidation state up to 4+, the modified integral Fe L_{23} white-line intensity ratio seems to be the most suitable approach in this case. The only limit of this last approach-

is that can be thickness dependent, a limitation which does not occur in the determination of oxidation states of clusters/atoms lying on the surface of a fiber. The contemporary application of all of these methods is usually feasible, if possible is thus convenient to compare all of them.

Chemical characterization

The chemical formulas of the two fibrous ferrierites, as determined from EMPA analyses are: $Fe^{3+}_{0.16}(K_{1.21}Mg_{2.11}Ca_{0.43}Na_{0.27})_{4.02}[Si_{29.20}Al_{6.89}O_{72}]\cdot 22.9H_2O$ (E%=+5.03, as defined in Gottardi and Galli 1985, with R=Si/(Si+Al)=0.80) for the BC sample and $Fe^{3+}_{0.19}(K_{2.41}Mg_{1.05}Ca_{0.28}Na_{0.06})_{3.80}[Si_{30.75}Al_{5.10}O_{72}]\cdot 20.0H_2O$ (E%=-0.58, with R=0.86) for the LN sample. The water content of the BC sample determined from the TG analysis (deposited as Supplementary Material) was 15.38 wt% and in agreement with the literature data (Wise and Tschernich 1976). Because it cannot be experimentally measured, the water content of the LN ferrierite is a theoretical value for the zeolite ferrierite species taken from the literature (Gottardi and Galli 1985; Rice et al. 1992). The diagenetic sample LN is more acidic (R=0.86) than the hydrothermal sample BC (R=0.80) with K as a dominant extraframework cation (DEC). As already found by Wise and Tschernich (1976), Mg is the DEC in the BC sample. Both samples display low Ca and Na contents. The chemistry is in agreement with the parameters reported by Passaglia and Sheppard (2001) for the ferrierite family.

Table 1 reports the mean values of the content of trace elements measured by spot analyses using LA-ICP-MS in the BC and LN samples with relative standard deviation. Data for fibrous erionite-Na is also reported (after Bloise et al. 2016), together with the concentrations commonly found in the human lungs (Vanoeteren et al. 1986). For some elements (e.g., Li, Be, Gd, Cs), concentrations were below the detection limits; whereas for others, the concentration (e.g., Sr and Ba) was higher than 1000 ppm and should, therefore, be considered as a minor element in the calculation of the chemical formula of the

sample. None of the metals considered as ecological and health risks (As, Co, Cr, Cu, Pb, Ni, Zn, V) are present in concentrations exceeding the threshold limits (Tóth et al. 2016). The major concentrations of metals relevant for the ecological and health risk are reported in Fig. 4. Data for Erionite-Na are also reported for comparison.

X-ray powder diffraction

The qualitative X-ray powder diffraction study evidenced that the BC sample is pure whereas the LN sample contains sanidine, mordenite, tridymite and smectite. Rice et al. (1992) also found feldspar, mordenite and an opal-CT as impurities in the sample. For the pure BC sample, the best indexing of the pattern was accomplished using the monoclinic model (space group $P2_1/n$) while the attempts using the orthorhombic models (e.g., *Immm*) failed in fitting all the peaks of the powder pattern. This was particularly evident for the doublets at ca. 4.00 Å (14.76 °2θ) and at ca. 2.95 Å (20.05 °2θ) which could only be correctly fitted with the monoclinic model (Fig. 5). Peak overlap with the impurity phases present in the LN sample prevented an accurate peak indexing analysis but the indications from the literature point to an orthorhombic structure model with space group *Immm* (Rice et al. 1994).

Vibrational spectroscopy

The micro-Raman spectrum of fibrous BC ferrierite (Fig. 6a) shows the typical bands displayed by massive ferrierite samples present in the RRUFF database (Lafuente et al. 2015). The most intense intra-tetrahedral band at 431 cm^{-1} is sensitive to the T-O-T angle and is found in the range 368 - 480 cm^{-1} for the zeolites with 5-membered rings like ferrierite (Dutta et al. 1988). The other major bands (Lercher and Jentys 2007) are at 330 cm^{-1} (pore opening inter-tetrahedral mode), 543 cm^{-1} (double ring inter-tetrahedral), 780 cm^{-1} (inter-tetrahedral symmetric stretching), and 1137 cm^{-1} (inter-tetrahedral

asymmetric stretching). The FTIR spectrum (Fig. 6b) shows the typical T-O-T antisymmetric and symmetric modes in the regions 1350-850 cm^{-1} and 850-620 cm^{-1}, respectively (Jacobs et al. 1993).

The modes of vibration of the water molecules present in the channels of the zeolite phase are visible in the region 3400-3000 cm^{-1} (stretching modes) and 1600-1630 cm^{-1} (bending modes) (Farmer 1974). The spectrum is nearly identical to that reported for massive ferrierite-Mg from Kamloops Lake, British Columbia present in the RRUFF database (Lafuente et al. 2015).

XPS

The XPS spectra of the BC and LN samples are plotted in Fig. 7. With the aim to reveal the Fe^{2+}/Fe^{3+} ratio at the surface of the fibers, XPS spectra were collected with a better resolution (1 eV) in the region 704 – 736 eV. Unfortunately, the Fe signal from the BC was too low to be detected whereas the signal from the LN sample allowed a quantitative analysis. Fe displays a complex assemblage with a prominent peak located approximately at 712 eV (inset in Fig. 7). The presence of satellite peaks indicates a higher content of Fe^{3+} with respect to Fe^{2+}. The calculated Fe^{3+}/Fe^{2+} ratio present at the surface of the LN ferrierite particles is 247/98 with 75 wt% represented by Fe^{3+} and 25 wt% by Fe^{2+}. This ratio is in concert with the data reported in Pollastri et al. (2015) for fibrous erionite, showing 84 wt% Fe^{3+} and 16 wt% Fe^{2+}.

EPR study

As far as the EPR analysis is concerned, a situation similar to that described in previous studies (Mattioli et al. 2016) was found. The positively charged CAT1 and CAT8 spin probes readily interact with the zeolite surface whose potential is negative due to the presence of the charged Si-O- and Al-O- sites and the polar Si-OH groups. However, CAT8 also bears a C8 hydrophobic chain and therefore shows surfactant properties. This spin probe is thus able to monitor by EPR the presence of low-

polarity sites (mainly Si-O-Si sites) and mimics the zeolite-surface interactions with components of the cell membranes. The EPR analysis was performed to evaluate the interactions occurring at the solid surface by analyzing the EPR spectra of the solid particles following exposure to the probe molecules in solution. In this case, micro-pools of probe solutions were trapped in the porosities, mainly those formed within fiber aggregates. The EPR spectra of these probes provided information about the interactions at the liquid/solid interfaces. Additional information was obtained by evaluating the percentage of adsorbed probe determined from the difference in intensities between the spectra obtained from stock solutions and the ones obtained from the filtered solution following equilibration with the zeolite fibers. Fig. 8 shows the EPR spectra of the solid particles after adsorption of CAT1 and CAT8 probes: A: BC + CAT1; B: BC + CAT8; C: LN + CAT1; D: LN + CAT8. As indicated with arrows in Fig. 8a,b, the spectra of CAT1 are constituted by two components. One is composed of three relatively narrow lines arising from CAT1 probes quite free to move in the solution pools in the zeolite-fibers interstices. The other component is termed "interacting", because the probes are slowly moving due to interactions with the zeolite surface at differently-polar sites. This determines the resolution of the anisotropies of the magnetic parameters. Spin-spin interactions between CAT1 probes adsorbed on sites close to each other in the BC sample provoke a line broadening and the interacting component appears as a broad single line. Fig. 8a,b also reports the computations which fit the interacting components. The calculated parameters (the percentages of the spectral components, the polarity parameter A_{zz}, the interaction parameter τ, and the spin-spin parameter line width LW) are listed in Table 2, together with the percentages of adsorbed probes. The parameters of both the interacting and the free components are reported. For CAT8 probes, the spectra are constituted by a single component due to interacting probes, and the fit lines in Fig. 8c,d are the corresponding computations. The parameters in Table 2 provide the following information:

-The percentage of adsorbed probes was very high for both zeolites regardless of probe type, but the highest value (95%) was found for CAT8 adsorbed on BC. This result suggests a preferential interaction of this surfactant probe with the BC surface, due to the occurrence of both hydrophilic and hydrophobic sites. Therefore, BC presents an overall less charged surface with more Si-O-Si groups if compared to LN;

-In agreement with the above finding, the calculated parameters of CAT8-containing samples are the same for BC and LN, except for the interaction parameter τ which is higher for LN with respect to BC. For the latter sample, the interactions with hydrophobic sites decreased the interaction strength at the polar sites;

-For CAT1, the relative percentage of the interacting component was higher for LN (91%) with respect to BC (85%), due to a more charged surface of the former. Furthermore, the presence of both hydrophilic and hydrophobic groups on the BC surface allowed a synergy between hydrophilic and hydrophobic interactions for CAT1 which increased the interaction parameter τ, but also increased the spin-spin parameter LW (24.5 G), due to interactions of CAT1 molecules adsorbed on adjacent surface groups, using both the more and less polar portions of the probe. For LN, both τ and LW were lower with respect to BC. These results are explained by the presence of a relatively high amount of positively charged ions, like Fe(III) ions, at the LN surface that partially hampered the interactions of the positively charged CAT1 group with the zeolite surface. The presence of these paramagnetic metal ions was proven by their characteristic EPR traces observed in the spectra recorded from the zeolite fibers (result not shown). Indeed, it was necessary to subtract these signals from the EPR spectra to extract information related to the interactions between the probe molecules and the LN surface.

-In line with the above findings, the free component in the EPR spectra of CAT1 at the LN surface is almost the same as the EPR spectrum of CAT1 in water. This indicates that the free probes trapped in

the water pools in the interstices of the zeolite fiber aggregates were not interacting with the zeolite surface; in other words, they are poorly affected by the zeolite surface due to the repulsion of the positively charged ions onto CAT1. Conversely, the free component of CAT1 in the inter-fiber voids showed slower mobility (τ=1.75 ns) in the BC aggregates with respect to the LN aggregates (τ=0.07 ns). This observation is in agreement with the assumption that free probe molecules inside the BC aggregates are affected by a negative zeolite-surface potential.

Specific surface area and ξ potential analysis

The specific surface areas (SSA) of the BC and LN samples were 11(1) and 7(1) m^2/g, respectively while the ESA (external surface area determined with the t-plot method) of the BC and LN samples conditioned at 350 °C was 35(1) and 26(1) m^2/g, respectively.

The ξ potential as a function of pH of the BC and LN samples are plotted in Fig. 9. The curves obtained in both distilled water and organic Gamble's modified solution SLF (Guldberg et al. 1998) are shown. In agreement with the literature data (Pollastri et al. 2014), the observed values of the ξ potential are all negative according to the model applied to zeolites (Pollastri et al. 2014). The trends are comparable to those observed for fibrous erionite (Pollastri et al. 2014) with a further decrease in the high pH range. As already observed in Pollastri et al. (2014) for fibrous erionite, the observed values of the ξ potential are less negative when the FER fibers are suspended in SLF.

Hydrothermal vs. diagenetic fibrous ferrierite

The two fibrous ferrierites investigated in this study represent samples of hydrothermal and diagenetic origin. Hydrothermal crystallization in voids of volcanic rocks is by far the most representative mode of occurrence. Instead, only a few examples of diagenetic occurrences of notable importance are described worldwide: tertiary rhyolitic pyroclastic rocks in Lovelock, Nevada USA

(Rice et al. 1992), pyroclastic units of the Tadami-machi Fukushima Japan (Hayakawa and Suzuki 1970), and tertiary tuffs in Yeongil Area Korea (Noh and Kim 1986). Besides the famous occurrences in the USA and Canada (Rice et al. 1992; Passaglia and Sheppard 2001), many other examples of fibrous radiating crystals of hydrothermal origin are described in the literature. A far from exhaustive list includes Hokkaido, Japan (Yajima et al. 1971); Monbetsu, Hokkaido, Japan (Matsubara et al. 1996); Nový Jičín, Western Carpathians (Urubek and Dolníček 2012). Although hydrothermal occurrences of fibrous ferrierites are widespread worldwide, they do not represent a health hazard as mass/volume concentration of the zeolite phase in the host rock is too low to justify industrial exploitation. On the other hand, in diagenetic occurrences, microcrystalline ferrierite is often the prevailing mineral phase in the rock making the zeolite-rich deposit viable for mining activity. If the rock is mined and used for agricultural and industrial applications (e.g., Townsend and Loizidou 1984), exposure for the workers and the population to fibrous ferrierite may eventually occur. To the best of the authors' knowledge, the investigated LN sample is the only example of diagenetic fibrous ferrierite mined and industrially used today.

Despite the same crystal habit, the hydrothermal BC and the diagenetic LN fibrous ferrierites display some differences. First of all, as zeolites, they show different chemistry. BC is a ferrierite-Mg with R=0.80 (Si/Al=4.2) while LN is a ferrierite-K with R=0.86 (Si/Al=6.0). The acidity of the zeolite species influences its biopersistence *in vivo* and, in turn, its toxicity. In fact, one of the key parameters of the fibers' toxicity paradigm (Pott et al., 1994) is the biopersistence, defined as the ability of a fiber (or particle in general) to be biodurable (to persist in the human body to physico-chemical processes such as dissolution, leaching, breaking, splitting) and to survive physiological clearance (Utembe et al., 2015). Si/Al framework ratio plays a key role in the dissolution mechanism in an acid environment (Hartman and Fogler, 2007), with the dissolution rate decreasing with increasing Si/Al ratio. Zeolite dissolution via dealumination can result in stoichiometric framework degradation, silicate precipitation,

partial dissolution of the silicate framework, or also in an intact silicate framework, in dependence of the initial Si/Al ratio (Hartman and Fogler, 2007). In fact, acid zeolites like erionite with Si/Al ratio > 2.5, show little to null dissolution in an acid environment, because dealumination does not eventually cause the collapse of the framework. LN is more acidic than BC and hence more biodurable and potentially more toxic/pathogenic than the hydrothermal counterpart.

The differences in the concentration of trace elements in the BC and LN samples (illustrated in Fig. 4), reflects their different origin. In general, the BC sample is poorer in trace elements but shows values of Sr and Ba >1000 ppm, which are much higher than the corresponding amounts found in the LN sample. On the other hand, the LN diagenetic sample is richer in V, Cr, Mn, Co, Cu, Zn, As, Rb, and Pb with respect to the hydrothermal BC sample.

The different chemistry (namely, the content of extraframework cations) is in agreement with their different crystal structures (not reported here) with the BC ferrierite-Mg showing a monoclinic $P2_1/n$ symmetry (this study) and the LN ferrierite-K an orthorhombic *Immm* symmetry (Rice et al. 1994).

Although both BC and LN samples contain ferrierite crystals with fibrous asbestiform crystals (Fig. 2) of breathable size (regulated fibers), their concentration is obviously higher in the LN sample where ferrierite is the prevailing mineral phase in the rock, and all of the crystals showing micrometric length. In the BC sample, most of the crystals exhibit sub-millimeter length, but the mass concentration of fibers is lower.

Similarly to fibrous erionite (Gualtieri et al. 2016), our results show that iron is not part of the zeolite structure but is associated with impurities, mostly concentrated at the surface of the fibers. In fact, in both samples, iron-rich (likely iron-oxides/hydroxides) nanophasic clusters, or microparticles, are found at the surface of the fibers (Fig. 3). As explained in Gualtieri et al. (2016), iron should not be found in the crystal lattice of natural zeolites because they are secondary products formed in open hydrologic systems or hydrothermal environments (see for example Sheppard and Hay 2001) where

ferrous iron present in the host rock is leached, oxidized and possibly re-precipitated as secondary iron-bearing phases (namely oxides/hydroxides). Even the hydrothermal synthesis in laboratory aimed at reproducing the natural systems shows that the majority of Fe^{3+} ions is not structural but belongs to precipitated impurities (Bart et al. 1983).

The measured ξ potential values indicate that the overall surface charge of the BC and LN samples in both distilled water and organic Gamble's modified solution SLF (Guldberg et al. 1998) are comparable and negative (Fig. 9). Notwithstanding, the EPR study showed that the surface characteristics of the two samples exhibited distinctive features, with the BC sample presenting a less charged surface (richer in Si-O-Si groups) if compared to LN. The presence of both hydrophilic and hydrophobic surface groups at the surface of BC allowed a close synergy between hydrophilic and hydrophobic interactions for CAT1. For LN, the presence of a slightly higher concentration of positively charged ions (namely Fe^{3+}) at the surface reduced the interaction of the positively charged CAT1 group with the zeolite surface.

The SSA of both the BC ferrierite samples conditioned at 105 °C and at 350 °C is greater than the corresponding samples of LN ferrierite because the BC sample is pure whereas the LN sample contains impurities with low SSA, such as sanidine.

Fibrous ferrierite vs. fibrous erionite

Based on mineralogical and physical-chemical data, we here discuss if fibrous ferrierite can be considered a potential health hazard like other asbestos minerals. To do so, the chemical-physical characters known to prompt adverse effects *in vivo* were compared to those of fibrous erionite taken as positive carcinogenic standard.

Both fibrous erionite and fibrous ferrierite can be found as major microcrystalline phase in diagenetic products (zeolite-rich rocks) that can be mined and exploited for various industrial

applications (namely building materials) exposing both workers and population to airborne fibers during mining operations, mineral processing, storage and later use of the market product, especially if it is sold as gravel or fine powder.

The two fibrous erionite and ferrierite can display asbestiform shape and can be released as airborne particulate fibers of breathable size, acting as regulated fibers according to the WHO (1997) counting criteria.

The values of the specific surface area (SSA) of the investigated fibrous ferrierites (see above) are comparable to those displayed by fibrous erionite (12.7(9) m^2/g for the sample conditioned at 105 °C and 39(2) m^2/g for the sample conditioned at 350 °C.

For both fibrous erionite and ferrierite, iron is not structural but associated with impurities at the surface of the fibers. According to the model described for fibrous erionite in Gualtieri et al. (2016), iron-rich impurities may dissolve during alveolar macrophage phagocytosis when the fibers are engulfed in the phago-lysosome sacks at pH = 4–4.5. Dissolution may leave a residue of iron atoms at specific sites anchored to the surface windows of the erionite channels. Specifically, one of these candidate active sites is located at the windows of the 6-membered rings (Fig. 10, right, showing the erionite framework along the **c** axis). These surface sites can be activated as iron low nuclearity groups prompting the H_2O_2-mediated release of free cyto- and genotoxic hydroxyl radicals responsible for adverse effects. Like for erionite, the ferrierite framework (Gottardi and Galli 1985) also possesses a candidate active site at the windows of the 6-membered rings (Fig. 10, left, showing the ferrierite framework along the **b** axis) and hence the model above can also be applied to this zeolite species.

As we have seen above, one of the key parameters of the fibers' toxicity paradigm is biopersistence. *In vitro* acellular studies of Gualtieri et al. (2018) showed that erionite-Na from Jersey is highly biodurable in contact with an alveolar macrophage phago-lysosome simulated lung fluid at pH = 4 and this can be one of the key factors in determining its high toxicity/pathogenicity potential. Because the

Si/Al ratio of Erionite-Na from Jersey is 2.8 (Gualtieri et al. 2016) and that of fibrous ferrierite samples is 4.2 for BC and 6.0 for LN, respectively, it is expected that ferrierite is even more biodurable than erionite in the intracellular environment.

The content of trace metals is another chemical-physical character that may contribute to prompt adverse effects *in vivo* of mineral fibers and should be considered in a model of toxicity/pathogenicity (Gualtieri et al. 2017). If we focus on the major metals considered of ecological and health risk: As, Co, Cr, Cu, Pb, Ni, Zn, V (Tóth et al. 2016), their concentration in the ferrierite and erionite-Na samples evidences some differences (Table 1 and Fig. 4). The BC ferrierite displays low concentrations that are comparable or lower to those of the LN ferrierite and erionite-Na. Hence, as far as the concentration of trace metals as potentially inducing toxicity/pathogenicity factor, the BC sample does not represent a hazard. The diagenetic LN ferrierite has a chemical trace that is more similar to diagenetic erionite-Na, but it shows a concentration of As and Pb lower than that of erionite-Na, Cr and Zn greater than erionite-Na, and comparable content of V.

It is very interesting to compare the interaction ability of the studied ferrierite samples, as inferred by the EPR analysis, with that of other fibrous zeolites such as erionite and offretite (Mattioli et al. 2016). The adsorbed percentage of probes was high for CAT1 (85%) and very high for CAT8 (87-95%) for the ferrierite samples. These values are significantly higher than those obtained for the other fibrous zeolites using CAT1 (~50-54% for erionite, 43.5% for offretite), while they are comparable using CAT8 (~85-99% for erionite, 96% for offretite). The greater interacting ability of ferrierite with respect the other fibrous zeolites is also confirmed, for CAT1, by the relative percentage of the interacting component, which is higher for both samples (Fer3 91%, Fer2 85%). The interacting strength measured by the correlation time for motion (the interaction parameter τ) is comparable for ferrierite and erionite fibers in respect of the polar sites, but the less polar sites (Si-O-Si) are better distributed at the ferrierite surface if compared to erionite surface.

This is a preprint, the final version is subject to change, of the American Mineralogist (MSA)
Cite as Authors (Year) Title. American Mineralogist, in press.
DOI: https://doi.org/10.2138/am-2018-6508

IMPLICATIONS

One of the most important implication of this work on the characterization of the mineralogical, chemical-physical parameters and surface activity of a hydrothermal fibrous ferrierite from Monte Lake British Columbia (Canada) and a diagenetic fibrous ferrierite from Lovelock Nevada (USA) is that fibrous ferrierite may be considered a potential health hazard, just like fibrous erionite. This claim is based on the experimental evidence that fibrous ferrierite and erionite share a number of common features: they can occur as major microcrystalline phase in minable diagenetic rocks; they may display asbestiform shape and disperse fibers of breathable size in the air; for both minerals, iron is not structural but is associated with impurities at the surface of the fibers that may eventually lead to the formation of surface active iron atoms at the window of 6-membered rings; being acid zeolites, the biodurability and hence the toxicity/pathogenicity potential of these fibrous minerals is high.

We have seen that there are differences in the nature, crystal chemistry and surface activity of the hydrothermal and diagenetic ferrierite samples with consequent differences in potential risk levels. For example, EPR data for the BC sample indicate the presence of hydrophilic (SiO-, AlO-, SiOH) and hydrophobic (Si-O-Si) interacting surface groups able to bind the charged CAT1 probes at close sites and attract the probes in the water pools formed into the fiber aggregates, but also offering a synergy between hydrophilic and hydrophobic interactions for CAT8 probes. A high percentage of CAT1 probes weakly interacting with the surface due to competition with metal ions was observed for LN surface. CAT8 probes were less adsorbed by LN surface if compared to BC, but the more charged surface provided a stronger binding strength for LN compared to BC.

It must be underlined that hydrothermal fibrous ferrierites are widespread worldwide but do not represent a health hazard as their occurrence in the host rocks represents just a beautiful singularity for the mineral collectors with little to null exposure risk for the population. On the contrary, deposits of

diagenetic fibrous ferrierite are not widespread, but they may host microcrystalline ferrierite in minable amounts. If the rock is mined and used for agricultural and industrial applications (e.g., Townsend and Loizidou 1984), the risk of exposure to fibrous ferrierite may be relevant for both workers and the population. To the knowledge of the authors, the LN sample is the only example of diagenetic fibrous ferrierite that is mined and industrially used today.

Another important implication of this work is that, based on the precautionary principle, fibrous ferrierite should be considered to undergo toxicity tests. To this aim, *in vitro* 2D and 3D toxicology screening (Linde et al. 2012) are in progress. The preliminary screening should later be integrated with *in vivo* acute and chronic tests if the toxicity screening is positive. This road map for the assessment of the toxicity/cancerogenicity potential of fibrous natural ferrierite may also be applied to synthetic fibrous counterparts that are commonly produced in laboratory or at industrial scale (Gögebakan et al. 2007).

ACKNOWLEDGMENTS

This research was conducted within the granted Italian National PROGETTO DI UNA UNITÀ DI RICERCA (PRIN) 2010–2011 –prot. 2010MKHT9B 004 “Interazione fra minerali e biosfera: conseguenze per l’ambiente e la salute umana”. Part of this work was taken from the bachelor thesis of M. Fanelli. This research was partially supported by the project No. LO1219 under the Ministry of Education of Czech Republic. S/TEM analyses were performed thanks to a Rotary Global Grant GG1640842 assigned to RV. The Principal Editor and two competent referees are kindly acknowledged for their comments and suggestions that certainly improved the quality of the manuscript.

REFERENCES CITED

Alberti, A., and Sabelli, C. (1987). Statistical and true symmetry of ferrierite: possible absence of straight T—O—T bridging bonds. Zeitschrift für Kristallographie-Crystalline Materials, 178(1-4), 249-256.

Baerlocher, C., McCusker, L.B., and Olson, D.H. (2007). Atlas of zeolite framework types. Elsevier.

Barca, D., and Trua, T. (2012) Magma emplacement at anomalous spreading ridge: constraints due to plagioclase crystals from basalts of Marsili seamount (Southern Tyrrhenian back-arc). Journal of Volcanology and Geothermal Research, 241–242, 61–77.

Bart, J. C. J., Burriesci, N., Cariati, F., Petrera, M., and Zipelli, C. (1983) A spectroscopic investigation of the iron distribution in zeolites derived from lipari pumice. Zeolites, 3(3), 226-232.

Bloise, A., Barca, D., Gualtieri, A. F., Pollastri, S., and Belluso, E. (2016) Trace elements in hazardous mineral fibres. Environmental Pollution, 216, 314-323.

Budil, D.E., Lee, S., Saxena, S., and Freed, J.H. (1996) Nonlinear-least-squares analysis of slow-motion EPR spectra in one and two dimensions using a modified Levenberg-Marquardt algorithm. Journal of Magnetic Resonance, Series A, 120, 155-89.

Carbone, M., Baris, Y. I., Bertino, P., Brass, B., Comertpay, S., Dogan, A.U., Gaudino, G., Jube, S., Kanodia, S., Partridge, C.R., Pass, H.I., Rivera, Z.S., Steele, I., Tuncer, M., Way, S., Yang, H., and Miller, A. (2011) Erionite exposure in North Dakota and Turkish villages with mesothelioma. Proceedings of the National Academy of Sciences, 108(33), 13618-13623.

Carbone, M., Kanodia, S., Chao, A., Miller, A., Wali, A., Weissman, D., Adjei, A., Baumann, F., Boffetta, P., Buck, B., de Perrot, M., Dogan, U., Gavett, S., Gualtieri, A.F., Hassan, R., Hesdorffer, M., Hirsch, F.R., Larson, D., Mao, W., Masten, S., Pass, H.I., Peto, J., Pira, E., Steele, I., Tsao, A., Woodard, G.A., Yang, H., Malik S. (2016) Consensus report of the 2015 Weinman International Conference on mesothelioma. Journal of thoracic oncology, 11(8), 1246-1262.

Dutta, P. K., and Del Barco, B. (1988) Raman spectroscopy of zeolite A: influence of silicon/aluminum ratio. The Journal of Physical Chemistry, 92(2), 354-357.

Farmer, V.C. (1974) Infrared spectra of minerals. Mineralogical society.

Fjellvåg, H., Lillerud, K. P., Norby, P., and Sørby, K. (1989) Structural properties of some ferrierite-type zeolites. Zeolites, 9(2), 152-158.

Göğebakan, Z., Yücel, H., and Culfaz, A. (2007) Crystallization field and rate study for the synthesis of Ferrierite. Industrial & Engineering Chemistry Research, 46(7), 2006-2012.

Goodman, B. S., and Pierson, M. P. (2010) Erionite, a naturally occurring fibrous mineral hazard in the tristate area of North Dakota, South Dakota, and Montana. In Geological Society of America Abstracts with Programs (Vol. 42, No. 5).

Gottardi, G., and Galli, E. (1985) Natural zeolites, 409 pp.

Graham, R. PD. (1918) On ferrierite, a new zeolitic mineral, from British Columbia. Royal Soc. Canada. Proc. and Trans., 3rd Series, 12, 185-190.

Gramlich-Meier, R., Meier, W. M., and Smith, B. K. (1984) On faults in the framework structure of the zeolite ferrierite. Zeitschrift für Kristallographie-Crystalline Materials, 169(1-4), 201-210.

Gramlich-Meier, R., Gramlich, V., and Meier, W. M. (1985) The crystal structure of the monoclinic variety of ferrierite. American Mineralogist, 70(5-6), 619-623.

Gualtieri, A. F., Gandolfi, N. B., Pollastri, S., Pollok, K., and Langenhorst, F. (2016) Where is iron in erionite? A multidisciplinary study on fibrous erionite-Na from Jersey (Nevada, USA). Scientific reports, 6.

Gualtieri, A.F., Mossman, B., and Roggli, V. (2017) Towards a general model for predicting the toxicity and pathogenicity of mineral fibres. Chapter 15 in: Mineral fibres: Crystal chemistry, chemical-physical properties, biological interaction and toxicity. EMU Notes in Mineralogy, 18, 501-532.

Gualtieri, A.F., Marchi, E., and Passaglia, E. (1999) Zeolite content and cation exchange capacity of zeolite-rich rocks. Studies in surface science and catalysis, 125, 707-713.

Gualtieri, A.F., Pollastri, S., Bursi Gandolfi, N., and Lassinantti Gualtieri, M. (2018) *In vitro* acellular dissolution of mineral fibers. A comparative study. Scientific Reports, submitted.

Guldberg, M., Christensen, V. R., Perander, M., Zoitos, B., Koenig, A. R., and Sebastian, K. (1998) Measurement of *in-vitro* fibre dissolution rate at acidic pH. The Annals of Occupational Hygiene, 42(4), 233-243.

Hayakawa, N., and Suzuki, S. (1970) Zeolitized Tuffs and Occurrence of Ferrierite in Tadami-machi, Fukushima Prefecture. Mining Geology, 20(102), 295-305.

Harper, M., Dozier, A., Chouinard, J., and Ray, R. (2017) Analysis of erionites from volcaniclastic sedimentary rocks and possible implications for toxicological research. American Mineralogist, 8(102), 1718-1726.

Hartman, R. L., and Fogler, H. S. (2007) Understanding the dissolution of zeolites. Langmuir, 23(10), 5477-5484.

Jacobs, W. P. J. H., De Haan, J. W., Van de Ven, L. J. M., and Van Santen, R. A. (1993) Interaction of ammonia with Broensted acid sites in different cages of zeolite Y as studied by proton MAS NMR. The Journal of Physical Chemistry, 97(40), 10394-10402.

Jones, A.G. (1959) Vernon map-area, British Columbia. Geological Survey Canada Memories, 296.

Kerr, I. S. (1966) Structure of ferrierite. Nature, 210(5033), 294.

Lafuente, B., Downs, R,T., Yang, H., and Stone, N. (2015) The power of databases: the RRUFF project. In: Highlights in Mineralogical Crystallography, T Armbruster and R M Danisi, eds. Berlin, Germany, W. De Gruyter, pp 1-30.

Lercher, J. A., and Jentys, A. (2007) Infrared and Raman spectroscopy for characterizing zeolites. Studies in surface science and catalysis, 168, 435-476.

Linde, N., Gutschalk, C. M., Hoffmann, C., Yilmaz, D., and Mueller, M. M. (2012) Integrating macrophages into organotypic co-cultures: a 3D in vitro model to study tumor-associated macrophages. PloS one, 7(7), e40058.

Malis, T., Cheng, S.C., Egerton R.F. (1988) EELS log-ratio technique for specimen-thickness measurement in the TEM. Journal of Electron Microscopy Technique, 8(2), 193-200.

Matsubara, S., Tiba, T., Kato, A., and Shimizu, M. (1996) Ferrierite from Monbetsu, Hokkaido, Japan. Mineralogical Journal, 18(4), 147-153.

Mattioli, M., Giordani, M., Dogan, M., Cangiotti, M., Avella, G., Giorgi, R., Dogan, A.U., and Ottaviani, M.F. (2016) Morpho-chemical characterization and surface properties of carcinogenic zeolite fibers. Journal of Hazardous Materials, 305, 140–148.

Noh, J.H., and Kim, S.J. (1986) Zeolites from tertiary tuffaceous rocks in Yeongil area, Korea. Studies in Surface science and catalysis, 28, 59-66.

Passaglia, E., and Sheppard, R. A. (2001) The crystal chemistry of zeolites. Reviews in mineralogy and geochemistry, 45(1), 69-116.

Pickering, I. J., Maddox, P. J., Thomas, J. M., and Cheetham, A. K. (1989) A neutron powder diffraction analysis of potassium-exchanged ferrierite. Journal of Catalysis, 119(1), 261-265.

Pollastri, S., Gualtieri, A. F., Gualtieri, M. L., Hanuskova, M., Cavallo, A., and Gaudino, G. (2014) The zeta potential of mineral fibres. Journal of hazardous materials, 276, 469-479.

Pollastri, S., D'Acapito, F., Trapananti, A., Colantoni, I., Andreozzi, G. B., and Gualtieri, A. F. (2015) The chemical environment of iron in mineral fibres. A combined X-ray absorption and Mössbauer spectroscopic study. Journal of hazardous materials, 298, 282-293.

Pott, F., Roller, M., Kamino, K., and Bellmann, B. (1994) Significance of durability of mineral fibers for their toxicity and carcinogenic potency in the abdominal cavity of rats in comparison with the low sensitivity of inhalation studies. Environmental health perspectives, 102(Suppl. 5), 145.

Rice, S. B., Papke, K. G., and Vaughan, D. E. (1992) Chemical controls on ferrierite crystallization during diagenesis of silicic pyroclastic rocks near Lovelock, Nevada. American Mineralogist, 77(3-4), 314-328.

Rice, S. B., Treacy, M. M. J., and Newsam, J. M. (1994) Shear faults in Lovelock ferrierite: An X-ray and electron diffraction analysis. Zeolites, 14(5), 335-343.

Rojac, T., Bencan A., Dražić, G., Sakamoto, N, Ursic, H., Jancar, B., Tavcar, G., Makarovic, M., Walker, J., Malic, B., Damjanovic, D. (2017) Domain-wall conduction in ferroelectric $BiFeO_3$ controlled by accumulation of charged defects.

Saini-Eidukat, B., and Triplett, J. W. (2014) Erionite and offretite from the Killdeer Mountains, Dunn County, North Dakota, USA. American Mineralogist, 99(1), 8-15.

Sheppard, R. A., and Hay, R. L. (2001) Formation of zeolites in open hydrologic systems. Reviews in Mineralogy and Geochemistry, 45(1), 261-275.

Tan, H., Verbeeck, J., Abakumov, A., and Van Tendeloo, G. (2012) Oxidation state and chemical shift investigation in transition metal oxides by EELS. Ultramicroscopy, 116, 24-33.

Tóth, G., Hermann, T., Da Silva, M. R., and Montanarella, L. (2016) Heavy metals in agricultural soils of the European Union with implications for food safety. Environment international, 88, 299-309.

Urubek, T., and Dolníček, Z. (2012) Ferrierit-Mg z kalcitové žíly v monchiquitu na lokalitě žilina u nového jičína (SlezskÁ Jednotka, Vnější Západní Karpaty). Geologické výzkumy na Moravě a ve Slezsku, 19(1-2).

Utembe, W., Potgieter, K., Stefaniak, A. B., and Gulumian, M. (2015) Dissolution and biodurability: Important parameters needed for risk assessment of nanomaterials. Particle and fibre toxicology, 12(1), 11.

Townsend, R. P., and Loizidou, M. (1984) Ion exchange properties of natural clinoptilolite, ferrierite and mordenite: 1. Sodium—ammonium equilibria. Zeolites, 4(2), 191-195.

Vanoeteren, C., Cornelis, R., and Verbeeck, P. (1986) Evaluation of trace elements in human lung tissue III. Correspondence analysis. Science of the total environment, 54, 237-245.

Vaughan, P.A. (1966) The crystal structure of the zeolite ferrierite. Acta Crystallographica, 21, 983-990.

Wise, W. S., and Tschernich, R. W. (1976) The chemical compositions and origin of the zeolites offretite, erionite, and levyne. American Mineralogist, 61(9-10), 853-863.

WHO (World Health Organization) (1997) Determination of airborne fiber number concentrations. Geneva, pp. 53.

Yajima, S., Nakamura, T., and Ishii, E. (1971) New occurrence of ferrierite. Mineral. Journal, 6, 343-364.

This is a preprint, the final version is subject to change, of the American Mineralogist (MSA)
Cite as Authors (Year) Title. American Mineralogist, in press.
DOI: https://doi.org/10.2138/am-2018-6508

FIGURE CAPTIONS

Fig. 1. A stereomicroscopic image of the hydrothermal sample from Monte Lake, British Columbia (BC) showing aggregates of acicular/fibrous crystals with a light orange color.

Fig. 2. Gallery of SEM pictures and relative EDS spot analysis of the ferrierite samples. (a) BC sample with prismatic ferrierite crystals; (b) BC sample with fibrous asbestiform shape ferrierite crystals; (c) BC sample with microparticles enriched in iron present at the surface of the fibers; (d) LN sample that also displays ferrierite crystals with fibrous asbestiform shape; (e) EDS spectrum of the microparticles present at the surface of the fibers witnessing an enrichment in iron; (f) EDS spectrum of the surface of the fibers away from the microparticles with no iron.

Fig. 3. Gallery of high-resolution TEM images and relative EELS spot analyses of the BC sample. (a) cluster of iron rich nanoparticles found at the surface of the zeolite fibers; (b) iron rich nanoparticles at the surface of the zeolite fibers; (c) relative EDS spectrum of the cluster (a) and individual nanoparticle (b), identical for the two cases; (d) EDS spectrum of the zeolite fibers where no iron peaks are seen; (e) HAADF image with a lighter region where iron rich nanoparticles occur with a magnification in (f); (g) Dual-EELS core-loss region spectrum collected to determine the iron oxidation state of iron. The detail of a cluster was digitally magnified (2×) and the presence of single atoms evidenced using a band pass filter with exponential decay.

Fig. 4. Concentration of metals (V, Cr, Mn, Co, Ni, Cu, Zn, As, Pb) relevant for the environmental and health risks for the BC (black) and LN (gray) ferrierites. Erionite-Na (dark gray) is also reported for comparison.

Fig. 5. Selected regions of the powder pattern of the BC ferrierite showing the two doublets at ca. 14.76 and 20.05 °2θ) indexed correctly with the monoclinic $P2_1/n$ model and not with the orthorhombic *Immm* model.

Fig. 6. Characterization of the BC sample using vibrational spectroscopy. (a) micro-Raman spectrum showing the typical bands displayed by massive ferrierite samples present in the RRUFF database (see text for details); (b) FTIR spectrum showing the typical T-O-T antisymmetric and symmetric modes in the regions 1350-850 cm^{-1} and 850-620 cm^{-1}, respectively (see text for details).

Fig. 7. XPS spectra of BC and LN fibrous ferrierites. The Fe_{2p} region is plotted in the box with a complex pattern showing the major peak at 712 eV. Satellite peaks indicate a higher content of Fe^{3+} with respect to Fe^{2+}.

Fig. 8. EPR spectra of the solid particles after adsorption of CAT1 and CAT8 probes: (a) BC + CAT1; (b) BC + CAT8; (c) LN + CAT1; (d) LN + CAT8. The fit is obtained from the computed interacting components. The main parameters of computation are listed in Table 2.

Fig. 9. Curves of the ξ potential of the BC and LN ferrierites in both distilled water and organic Gamble's modified solution (SLF). Legend: white points are the measurements in distilled water at 37 °C; gray points are the measurements in SLF at 37 °C; circles refer to the BC sample and triangles refer to the LN sample.

Fig. 10. The position of low nuclearity iron atoms at the surface of the erionite (right) and ferrierite (left) channels. In both zeolite species, the sites are located at the windows of 6-membered rings. These

secondary building units are found along the **c** axis in the erionite framework (right) and along the **b** axis in the ferrierite framework (left).

Table 1. Trace elements concentration (in ppm) of various asbestos samples. The data of BC and LN samples are mean values of seven spot analyses executed by LA-ICP-MS.

Element	Elements in human lungs*	BC	S.D.	LN	S.D.	Erionite-Na Jersey**
Li	n.d.	n.d.	n.d.	5.61	1.06	4.45
Be	0.03	n.d.	n.d.	n.d.	n.d.	1.22
V	0.50	2.91	1.87	39.5	5.07	36.34
Cr	0.50	4.09	0.4	20.4	1.14	1.70
Mn	3.00	47.1	11.4	117	31	45.30
Co	0.10	0.40	0.23	0.84	0.16	0.78
Ni	1.00	2.42	1.21	2.32	0.81	1.72
Cu	5.00	0.36	0.13	3.74	1.59	1.90
Zn	30.00	8.62	5.69	114	13.06	9.66
As	0.10	2.45	0.92	3.65	1.6	44.50
Rb	10.00	64.1	11.50	173	34.70	39.51
Sr	1.00	1841	1044	429	70.90	222.00
Ba	>1.10	1251	730	74.9	14	393.00
Pb	0.50	0.48	0.14	18.9	3.81	25.22
U	0.01	0.05	0.01	7.39	2.32	1.10
Sc	n.d.	1.48	0.49	4.92	0.68	1.58
Y	n.d.	0.48	0.10	32	7.98	18.21
La	n.d.	n.d	n.d	35.9	10.08	65.60
Ce	n.d.	0.04	0.01	84	26.14	192.90
Pr	n.d.	n.d	n.d.	13.93	4.11	15.00
Nd	n.d.	0.33	0.26	36.9	11.09	33.30
Sm	n.d.	0.13	0.04	9.7	2.67	10.15
Eu	n.d.	0.16	0.04	0.26	0.02	1.30
Gd	n.d.	n.d.	n.d.	8.38	2.10	9.02
Tb	n.d.	0.02	0.01	1.44	0.29	1.15
Dy	n.d.	0.27	0.07	13.13	2.38	6.16
Ho	n.d.	0.12	0.09	1.45	0.39	1.13
Er	n.d.	0.13	0.02	4.13	0.95	3.30
Tm	n.d.	0.02	0.01	0.53	0.13	0.44
Yb	n.d.	0.11	0.01	2.23	0.52	2.45
Lu	n.d.	0.05	0.02	0.57	0.10	0.32
Th	n.d.	0.12	0.01	19.3	3.50	6.91
Sb	0.10	0.12	0.01	0.85	0.54	1.15
Cs	n.d.	n.d.	n.d.	n.d.	n.d.	2.00

*Indicative baseline data for some trace elements in normal human lung tissues (Vanoeteren et al. 1986);

**from Bloise et al. 2016; S.D. = standard deviation; n.d. = not detected.

Table 2. Main parameters of computation – percentages of the spectral components, polarity parameter A_{zz}, interaction parameter τ, spin-spin parameter LW (line width) - and percentages of adsorbed probes.

Sample	Probe	Adsorbed%	Component%	A_{zz} (G)	τ (ns)	LW (G)
BC	CAT1	85	85	37.5	5.5	24.5
			15	38.7	1.75	1.8
	CAT8	95	100	39	4.7	10
LN	CAT1	85	91	37.5	2.45	4.5
			9	39.2	0.07	0.4
	CAT8	87	100	39	5.9	10

This is a preprint, the final version is subject to change, of the American Mineralogist (MSA)
Cite as Authors (Year) Title. American Mineralogist, in press.
DOI: https://doi.org/10.2138/am-2018-6508

Is fibrous ferrierite a potential health hazard?

Characterization and comparison with fibrous erionite

by ALESSANDRO F. GUALTIERI

Table 1. Trace elements concentration (in ppm) of various asbestos samples. The data of BC and LN samples are mean values of seven spot analyses executed by LA-ICP-MS.

Element	Elements in human lungs*	BC	S.D.	LN	S.D.	Erionite-Na Jersey**
Li	n.d.	n.d.	n.d.	5.61	1.06	4.45
Be	0.03	n.d.	n.d.	n.d.	n.d.	1.22
V	0.50	2.91	1.87	39.5	5.07	36.34
Cr	0.50	4.09	0.4	20.4	1.14	1.70
Mn	3.00	47.1	11.4	117	31	45.30
Co	0.10	0.40	0.23	0.84	0.16	0.78
Ni	1.00	2.42	1.21	2.32	0.81	1.72
Cu	5.00	0.36	0.13	3.74	1.59	1.90
Zn	30.00	8.62	5.69	114	13.06	9.66
As	0.10	2.45	0.92	3.65	1.6	44.50
Rb	10.00	64.1	11.50	173	34.70	39.51
Sr	1.00	1841	1044	429	70.90	222.00
Ba	>1.10	1251	730	74.9	14	393.00
Pb	0.50	0.48	0.14	18.9	3.81	25.22
U	0.01	0.05	0.01	7.39	2.32	1.10
Sc	n.d.	1.48	0.49	4.92	0.68	1.58
Y	n.d.	0.48	0.10	32	7.98	18.21
La	n.d.	n.d	n.d	35.9	10.08	65.60
Ce	n.d.	0.04	0.01	84	26.14	192.90
Pr	n.d.	n.d	n.d.	13.93	4.11	15.00
Nd	n.d.	0.33	0.26	36.9	11.09	33.30
Sm	n.d.	0.13	0.04	9.7	2.67	10.15
Eu	n.d.	0.16	0.04	0.26	0.02	1.30
Gd	n.d.	n.d.	n.d.	8.38	2.10	9.02
Tb	n.d.	0.02	0.01	1.44	0.29	1.15
Dy	n.d.	0.27	0.07	13.13	2.38	6.16
Ho	n.d.	0.12	0.09	1.45	0.39	1.13
Er	n.d.	0.13	0.02	4.13	0.95	3.30

Tm	n.d.	0.02	0.01	0.53	0.13	0.44
Yb	n.d.	0.11	0.01	2.23	0.52	2.45
Lu	n.d.	0.05	0.02	0.57	0.10	0.32
Th	n.d.	0.12	0.01	19.3	3.50	6.91
Sb	0.10	0.12	0.01	0.85	0.54	1.15
Cs	n.d.	n.d.	n.d.	n.d.	n.d.	2.00

*Indicative baseline data for some trace elements in normal human lung tissues (Vanoeteren et al. 1986);

**from Bloise et al. 2016; S.D. = standard deviation; n.d. = not detected.

This is a preprint, the final version is subject to change, of the American Mineralogist (MSA)
Cite as Authors (Year) Title. American Mineralogist, in press.
DOI: https://doi.org/10.2138/am-2018-6508

Is fibrous ferrierite a potential health hazard?

Characterization and comparison with fibrous erionite

by ALESSANDRO F. GUALTIERI

Table 2. Main parameters of computation – percentages of the spectral components (accuracy ± 1%)[a], polarity parameter A_{zz} (accuracy ± 0.1 G)[a], interaction parameter τ (accuracy ± 0.05 ns)[a], spin-spin parameter LW (line width, accuracy ± 0.1 G)[a] - and percentages of adsorbed probes (accuracy ± 1%)[a].

Sample	Probe	Adsorbed%	Component%	A_{zz} (G)	τ (ns)	LW (G)
BC	CAT1	85	85	37.5	5.5	24.5
			15	38.7	1.75	1.8
	CAT8	95	100	39	4.7	10
LN	CAT1	85	91	37.5	2.45	4.5
			9	39.2	0.07	0.4
	CAT8	87	100	39	5.9	10

[a]The accuracy was determined by spectral computation: values higher or lower than those within the indicated accuracy provided a worse fitting between the experimental and the computed spectra.

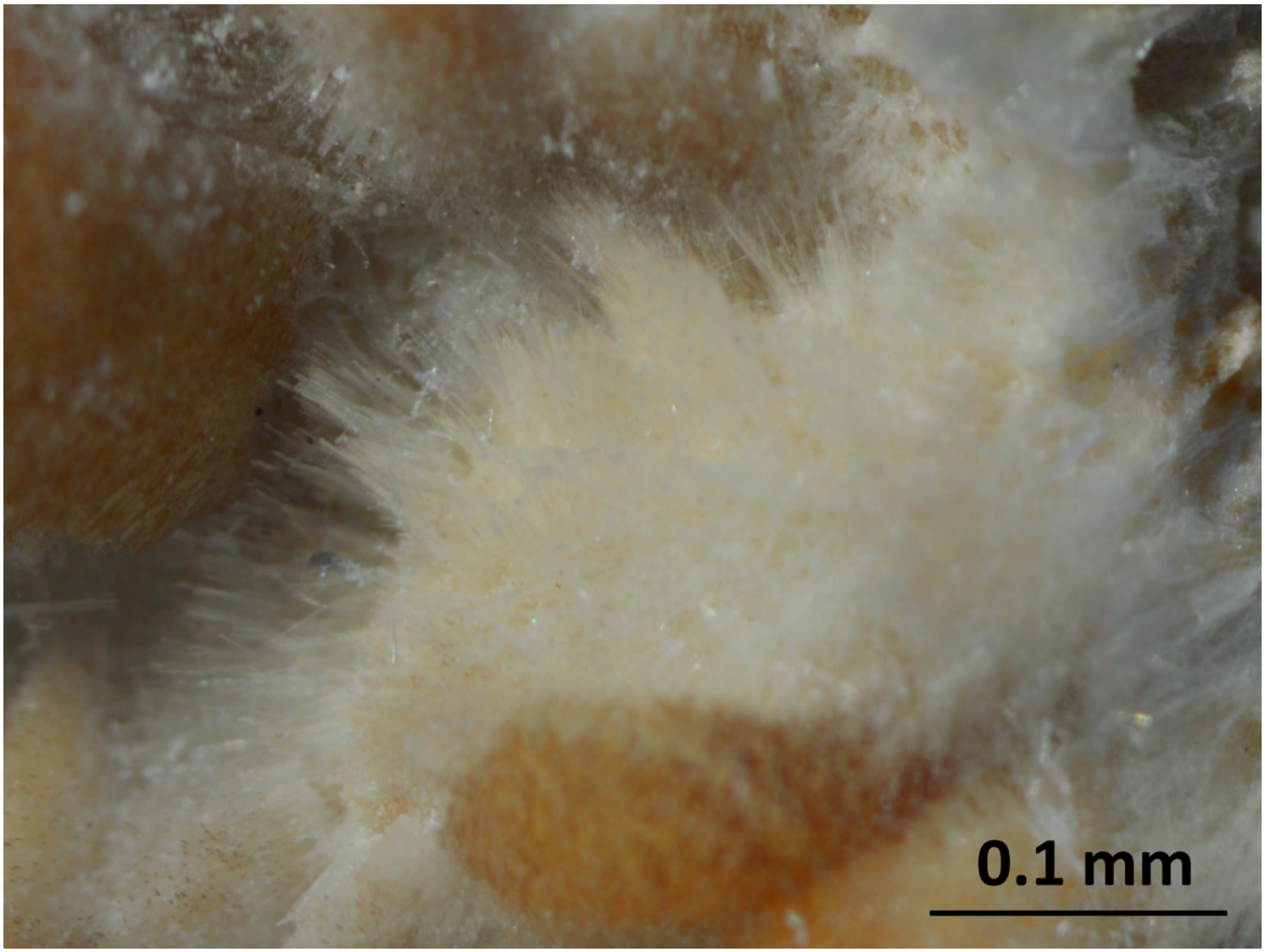

This is a preprint, the final version is subject to change, of the American Mineralogist (MSA)
Cite as Authors (Year) Title. American Mineralogist, in press.
DOI: https://doi.org/10.2138/am-2018-6508

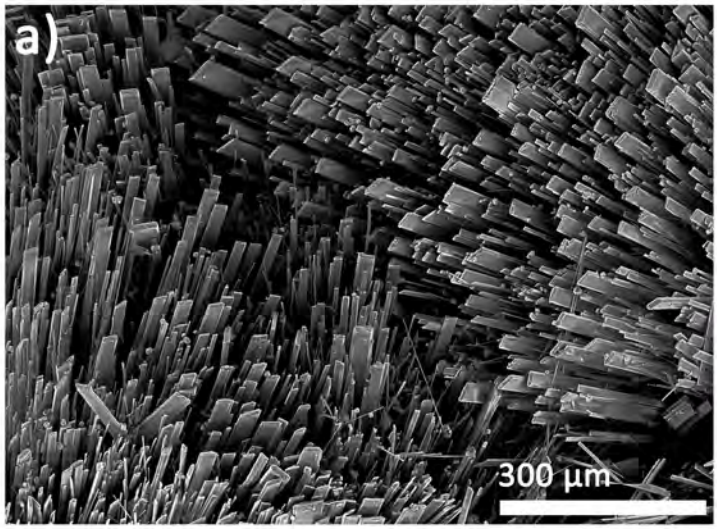

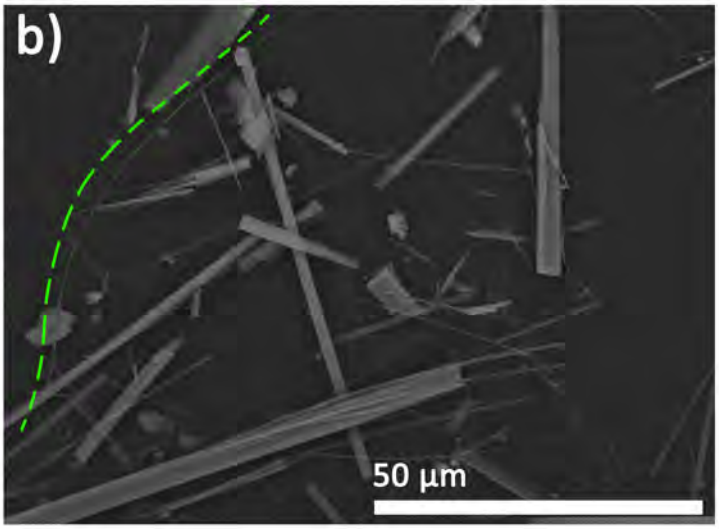

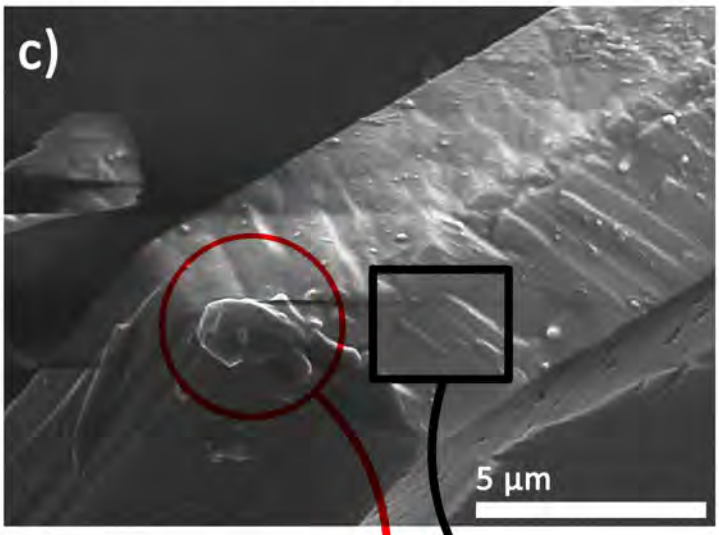

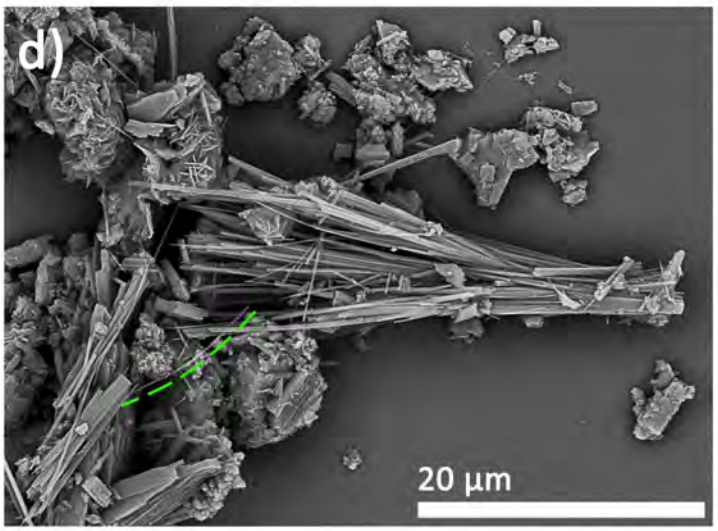

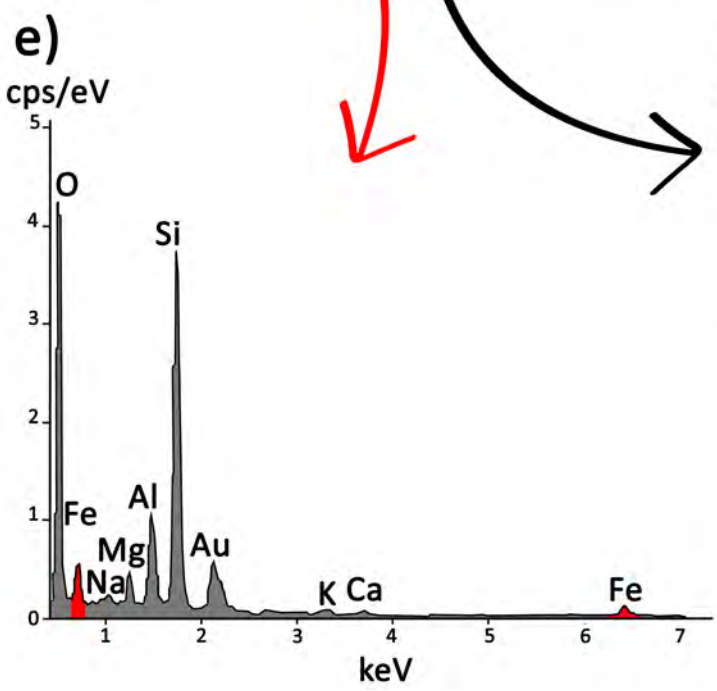

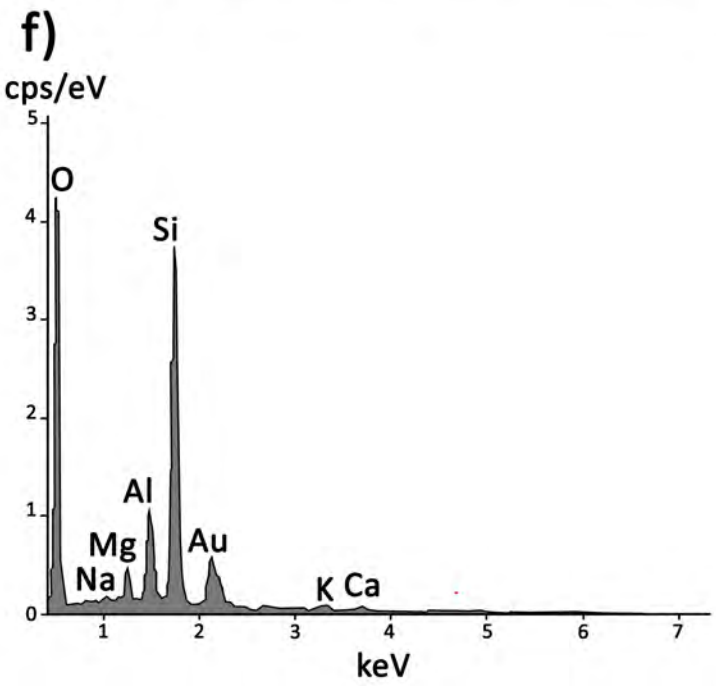

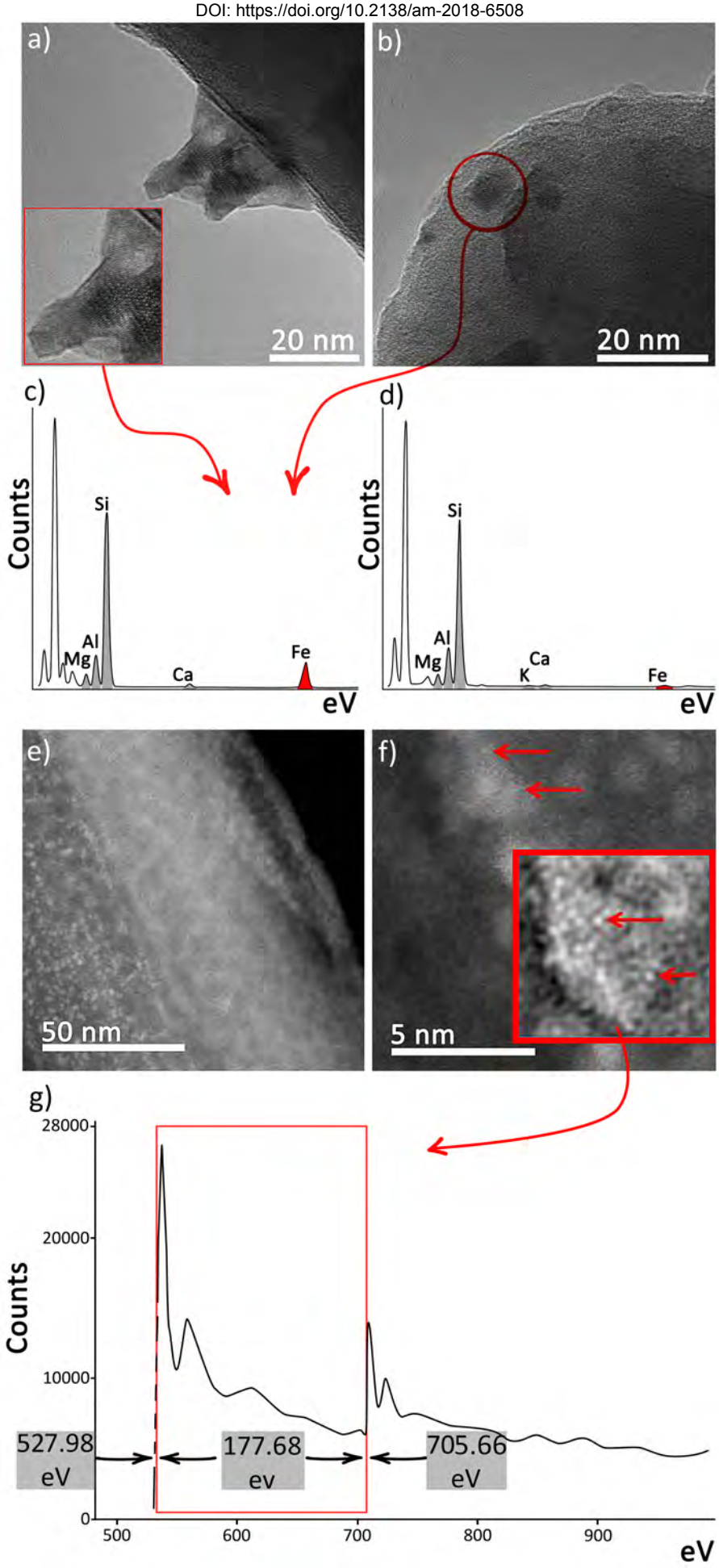

This is a preprint, the final version is subject to change, of the American Mineralogist (MSA)
Cite as Authors (Year) Title. American Mineralogist, in press.
DOI: https://doi.org/10.2138/am-2018-6508

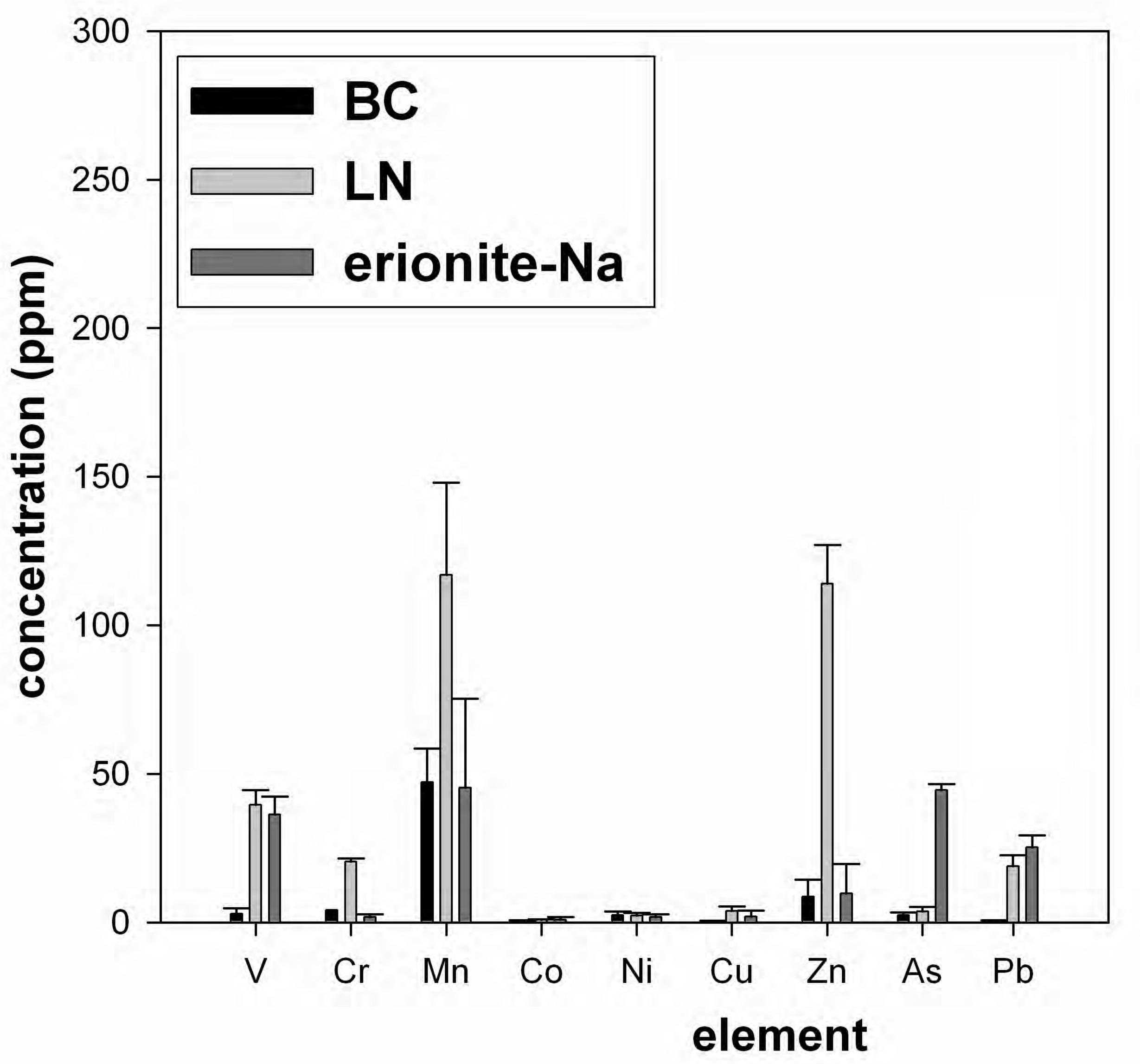

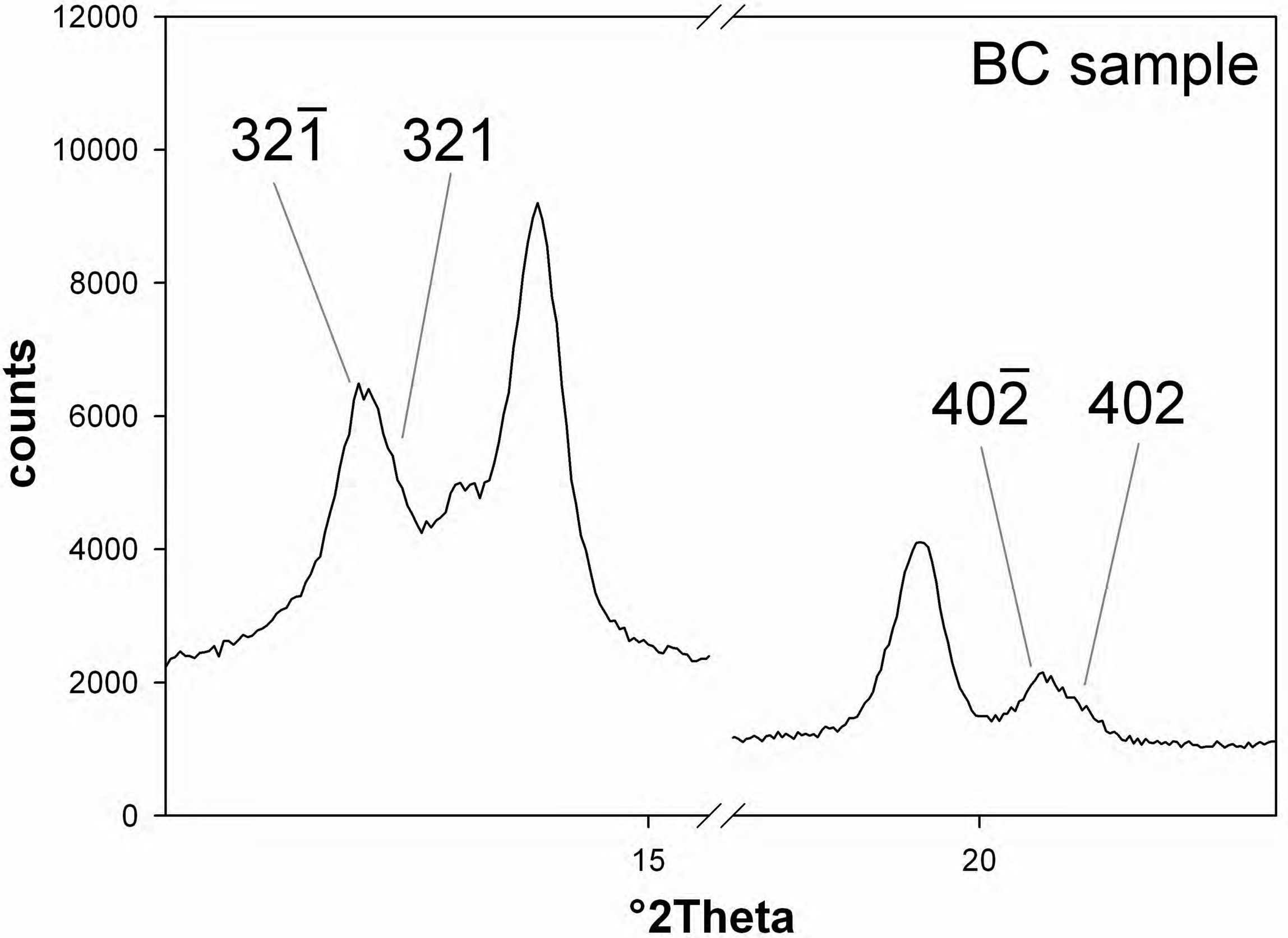

This is a preprint, the final version is subject to change, of the American Mineralogist (MSA)
Cite as Authors (Year) Title. American Mineralogist, in press.
DOI: https://doi.org/10.2138/am-2018-6508

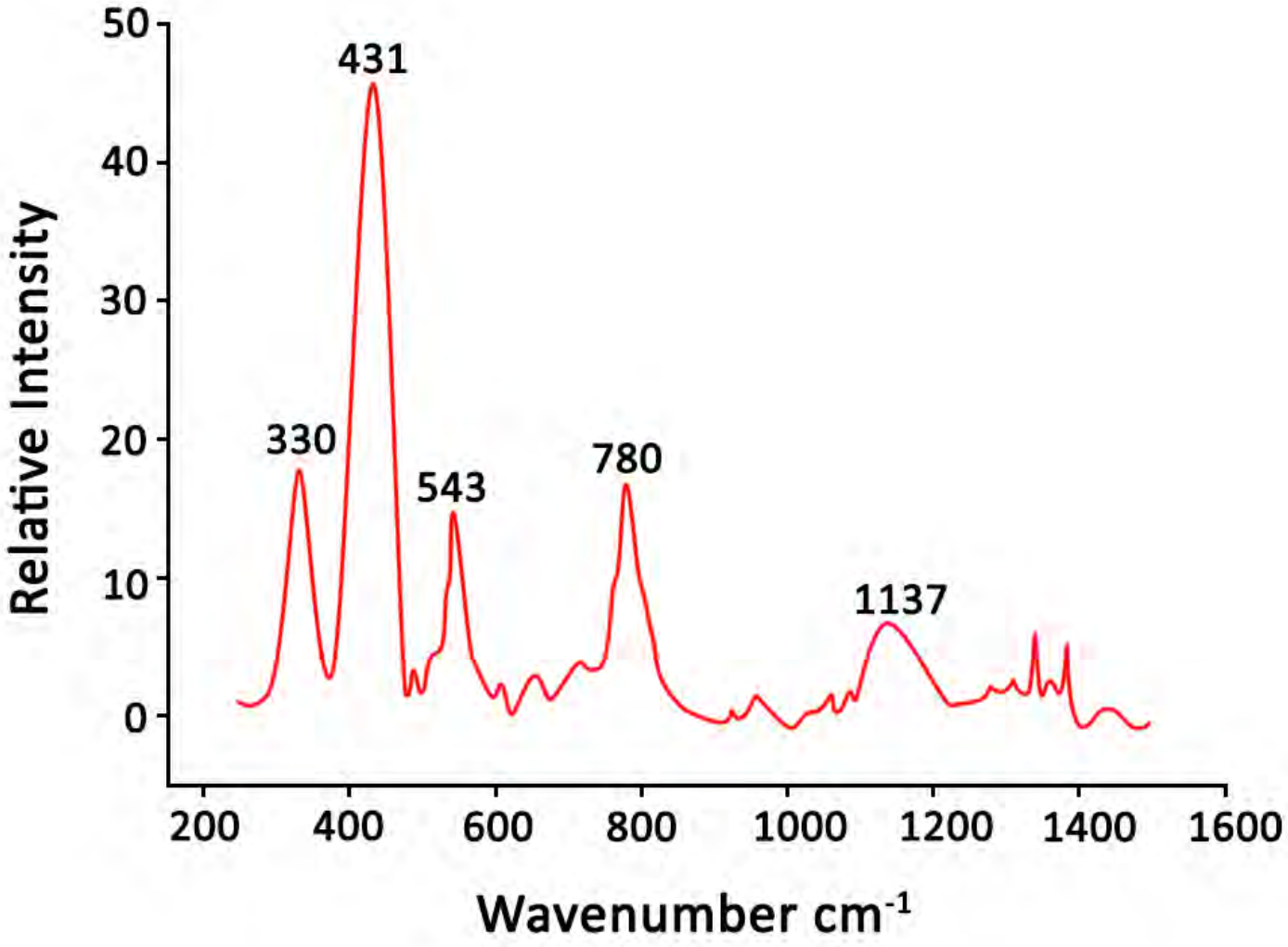

This is a preprint, the final version is subject to change, of the American Mineralogist (MSA)
Cite as Authors (Year) Title. American Mineralogist, in press.
DOI: https://doi.org/10.2138/am-2018-6508

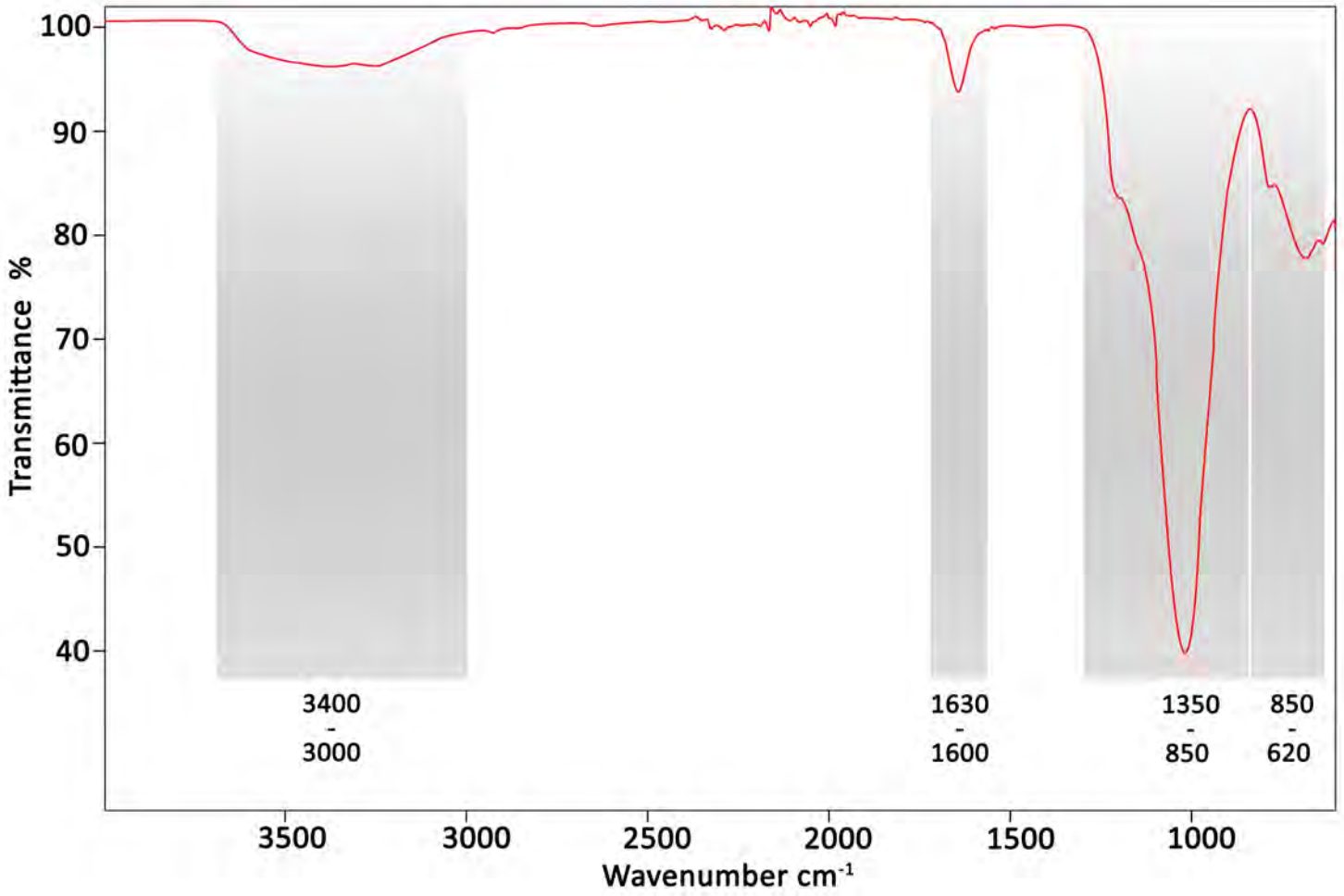

This is a preprint, the final version is subject to change, of the American Mineralogist (MSA)
Cite as Authors (Year) Title. American Mineralogist, in press.
DOI: https://doi.org/10.2138/am-2018-6508

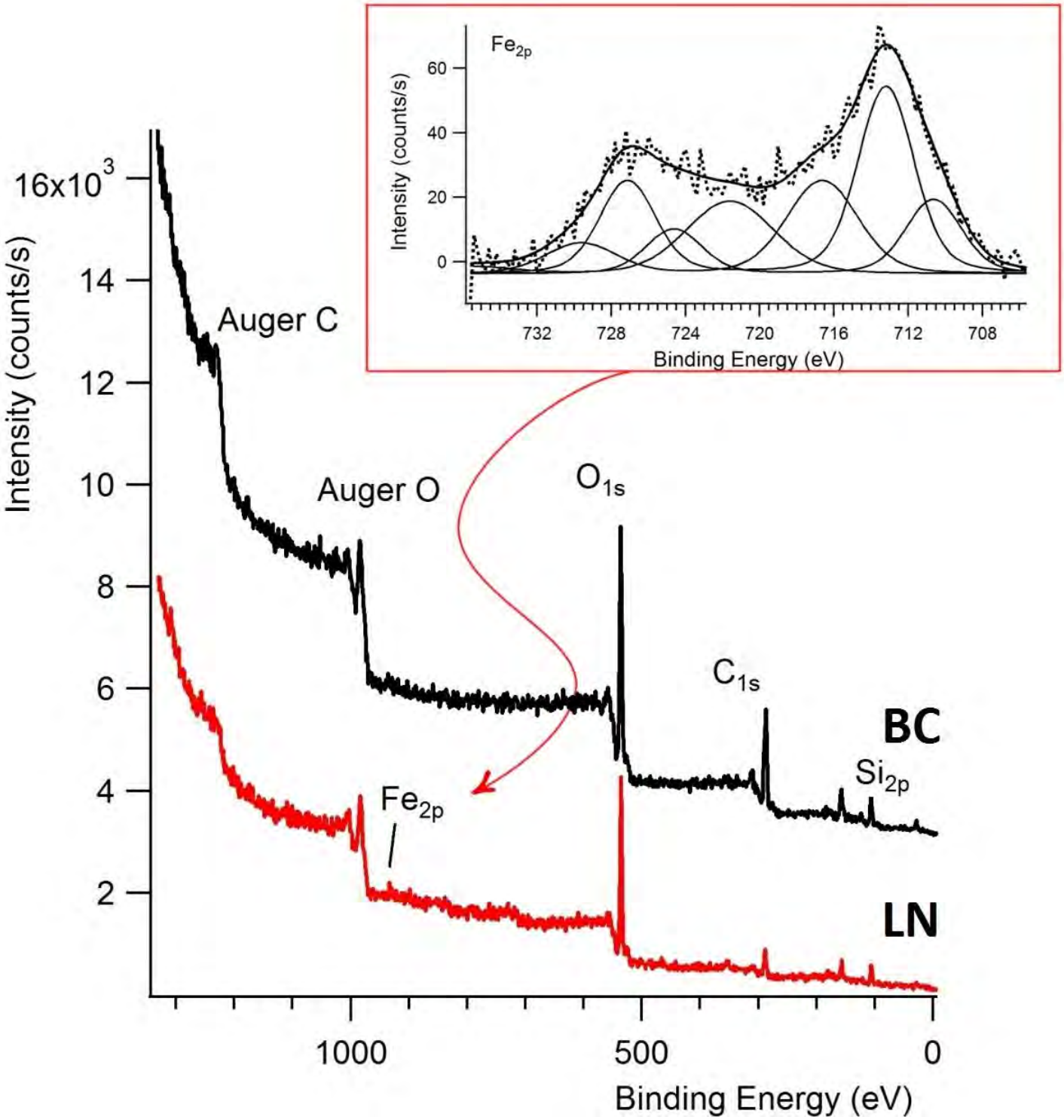

This is a preprint, the final version is subject to change, of the American Mineralogist (MSA)
Cite as Authors (Year) Title. American Mineralogist, in press.
DOI: https://doi.org/10.2138/am-2018-6508

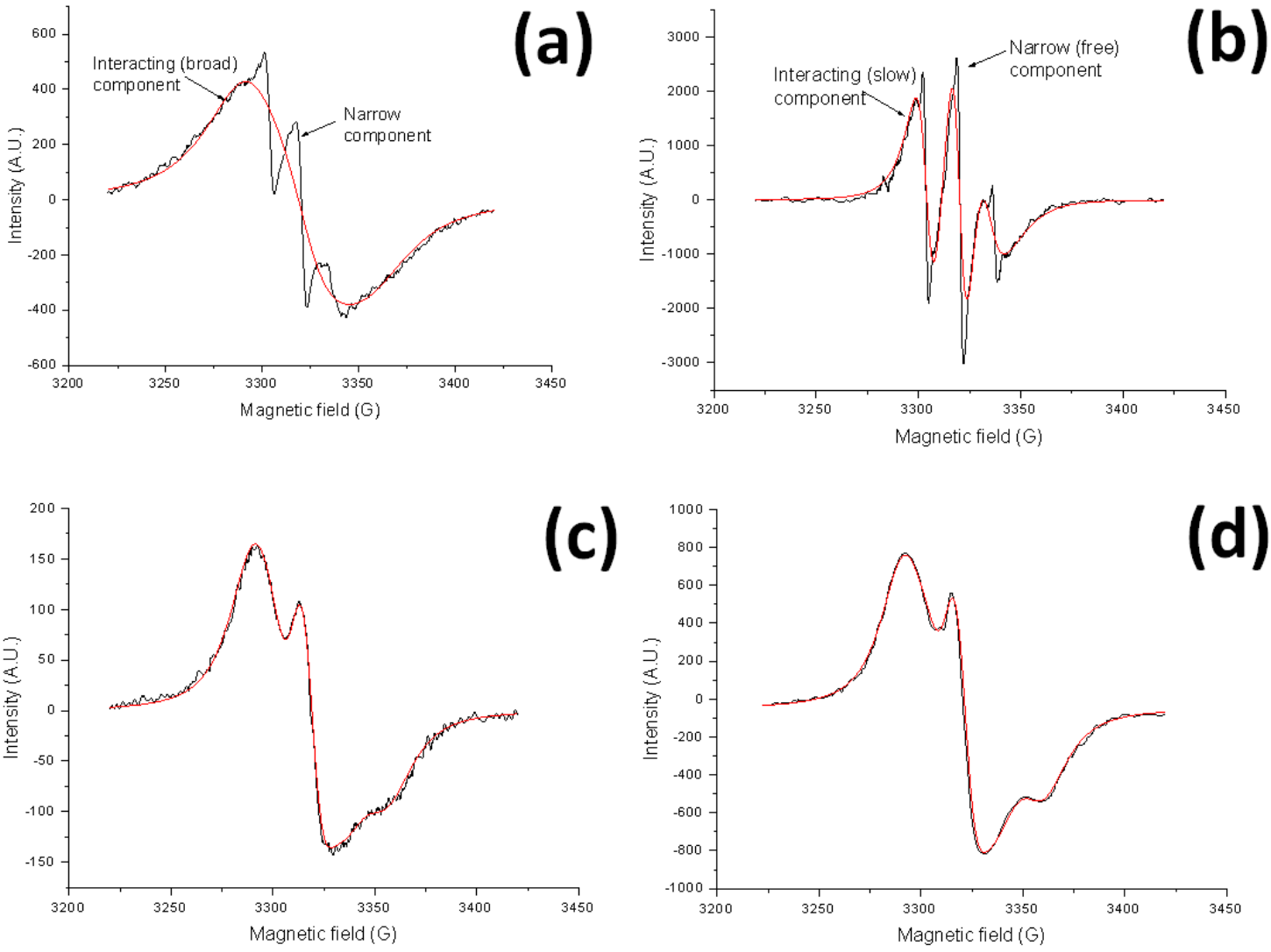

This is a preprint, the final version is subject to change, of the American Mineralogist (MSA)
Cite as Authors (Year) Title. American Mineralogist, in press.
DOI: https://doi.org/10.2138/am-2018-6508

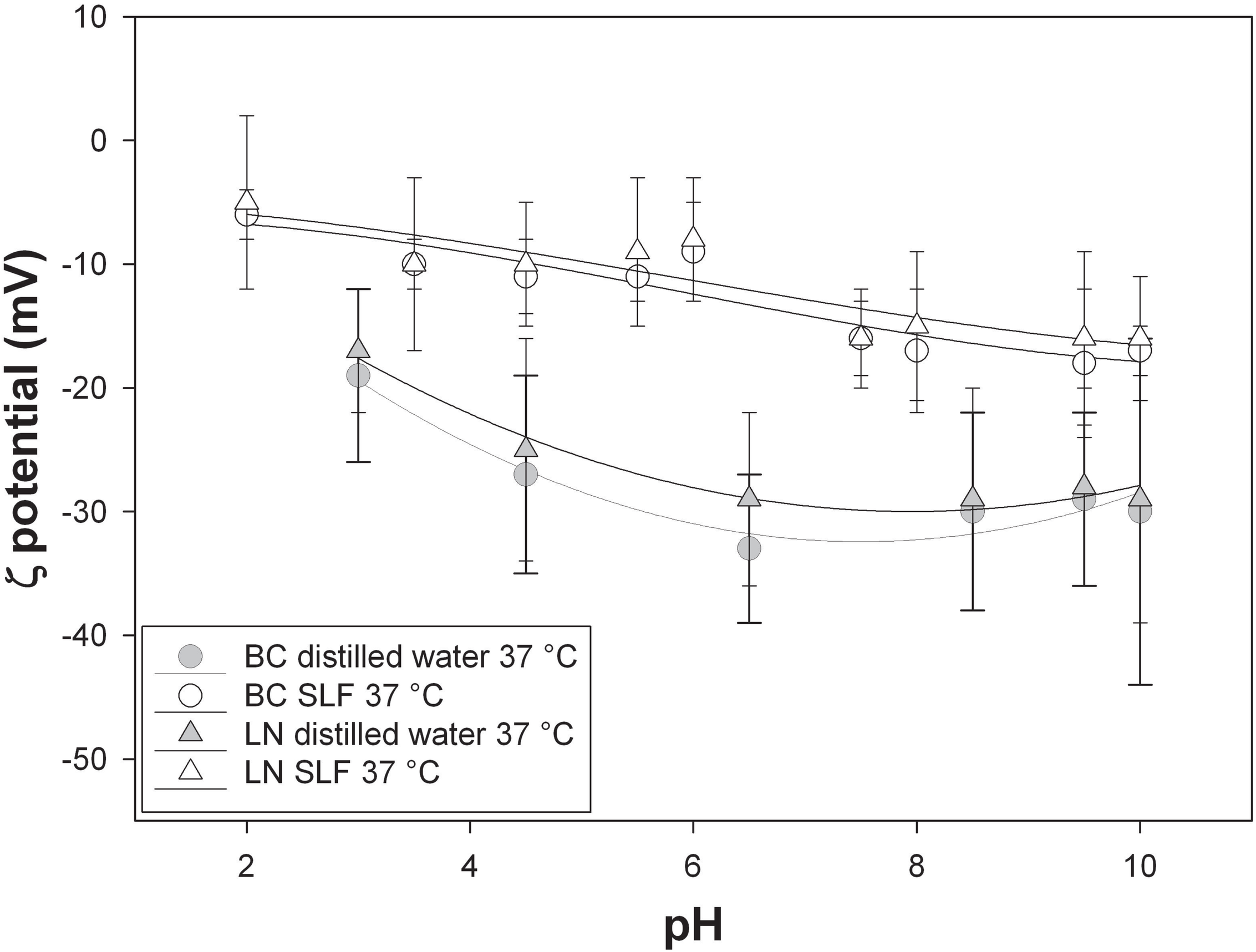

This is a preprint, the final version is subject to change, of the American Mineralogist (MSA)
Cite as Authors (Year) Title. American Mineralogist, in press.
DOI: https://doi.org/10.2138/am-2018-6508